The Astrophysical Journal, 998:48 (23pp), 2026 February 10 https://doi.org/10.3847/1538-4357/ae2fb1

Tracking the Assembly of Supermassive Black Holes: A Comparison of Diverse Models across Cosmic Time

Antonio J. Porras-Valverde[1], Angelo Ricarte[2], Priyamvada Natarajan[1,2,3], Rachel S. Somerville[4], Austen Gabrielpillai[5], and L. Y. Aaron Yung[6]

[1] Department of Astronomy, Yale University, P.O. Box 208101, New Haven, CT 06520, USA; antonio.porras@yale.edu
[2] Black Hole Initiative, Harvard University, Cambridge, MA 02138, USA
[3] Department of Physics, Yale University, P.O. Box 208121, New Haven, CT 06520, USA
[4] Center for Computational Astrophysics, Flatiron Institute, 162 5th Avenue, New York, NY 10010, USA
[5] The City University of New York, 365 5th Avenue, New York, NY 10016, USA
[6] Space Telescope Science Institute, 3700 San Martin Drive, Baltimore, MD 21218, USA

Received 2025 March 31; revised 2025 December 16; accepted 2025 December 17; published 2026 February 3

Abstract

Galaxies grow alongside central supermassive black holes (SMBHs) through fueling and feedback. However, the origins of this coevolution remain unclear and vary across modeling frameworks. Using semianalytic models (SAMs), we trace SMBH mass assembly across $M_{\rm BH} \sim 10^{6-10}\,M_\odot$. We find significant discrepancies between observations and physics-based models of the local black hole mass function (BHMF), likely from differences in the stellar mass function and scaling relations used to infer the BHMF. Most physics-based models agree at $z \sim 1$–4 and broadly match the JWST broad-line active galactic nucleus (AGN) BHMFs at $z = 4$–5. These models also reproduce the observed bolometric AGN luminosity evolution, except the SAM DARK SAGE, which predicts an excess. Interestingly, this pronounced "knee" in the bolometric AGN luminosity function predicted by DARK SAGE around $L_{\rm bol} \sim 10^{46}$ erg s^{-1} is consistent with the inferred abundance and luminosity of "little red dots" at $z = 5$–6, under the assumption that they are powered entirely by AGN activity. In contrast to other models, DARK SAGE deploys multiple growth channels for SMBHs that include mergers, hot-mode accretion, merger-driven cold-accretion, and secular-instability-driven accretion. We analyze the black hole mass buildup and accretion histories in DARK SAGE, which, unlike other models, also allows for super-Eddington accretion, and we find that, on average, SMBHs primarily grow through secular disk instabilities and merger-driven cold gas accretion modes. We also find that black hole mergers contribute the majority of the growth of ∼60% of the total mass budget only for the most massive SMBHs by $z = 0$.

Unified Astronomy Thesaurus concepts: Astrophysical black holes (98); Galaxy formation (595)

1. Introduction

Observations of nearby galaxies have shaped the consensus that most-massive galaxies host at least one central supermassive black hole (SMBH; 10^6–$10^{10}\,M_\odot$; J. Kormendy & D. Richstone 1995; J. Kormendy & L. C. Ho 2013). Several observational studies have established correlations between SMBH mass and the properties of their host elliptical galaxies such as the stellar velocity dispersion (using the $M_{\rm BH}$–σ relation; K. Gebhardt et al. 2000; D. Merritt & L. Ferrarese 2001; S. Tremaine et al. 2002), luminosity (R. J. McLure & J. S. Dunlop 2001, 2002), Sérsic index (A. W. Graham et al. 2001, 2007), bulge mass (J. Magorrian et al. 1998; A. Marconi & L. K. Hunt 2003; N. Häring & H.-W. Rix 2004), and binding energy (M. C. Aller & D. O. Richstone 2007; P. F. Hopkins et al. 2007a). These scaling relations suggest that the coevolution between SMBHs and elliptical galaxies is closely linked, primarily regulated by various factors such as active galactic nucleus (AGN) feedback. It is hypothesized that black holes grow by accreting gas during "active" phases, possibly fueled by a major merger of gas-rich galaxies, until the energy from the SMBH feedback expels the gas and halts the accretion process (J. Silk & M. J. Rees 1998; A. C. Fabian 1999; M. C. Begelman & B. B. Nath 2005; N. Murray et al. 2005).

Many models have connected SMBH growth, the quasar phase, and galaxy evolution (M. G. Haehnelt et al. 1998; M. G. Haehnelt & G. Kauffmann 2000; G. Kauffmann & M. Haehnelt 2000; M. Volonteri et al. 2003; J. S. B. Wyithe & A. Loeb 2003; A. Cattaneo et al. 2005; T. Di Matteo et al. 2008; R. S. Somerville et al. 2008; C. M. Booth & J. Schaye 2009). Although it appears that AGN feedback may play a critical role in balancing the growth of both SMBHs and galaxies, the mechanisms that fuel SMBH growth are plausibly diverse. Gas-rich galaxies that undergo major mergers may drive quasar activity at high redshifts, leading to the growth of the most-massive SMBHs (e.g., P. Kroupa et al. 2020). However, only accounting for major mergers does not yield the observed number of faint X-ray AGNs (F. Marulli et al. 2007). Instead, secular accretion of gas through internal galactic processes may fuel these dimmer, lower-mass AGNs at lower redshifts (L. Ciotti & J. P. Ostriker 2001; P. F. Hopkins & L. Hernquist 2006). Observational evidence points to AGNs being located in late-type galaxies up to $z \approx 1$ (O. Guyon et al. 2006; J. M. Gabor et al. 2009). The X-ray luminosity function from the AGNs in these galaxies suggests that internal instabilities may contribute significantly to the overall SMBH accretion history (A. Georgakakis et al. 2009).

Given the observed coevolution between SMBHs and galaxies, the black hole mass function (BHMF) offers valuable information about the primary fueling mechanisms responsible for black hole growth. Unfortunately, two overarching complications make observational measurements of the BHMF difficult: survey incompleteness, which relies on a flux limit, and SMBH mass uncertainty. Currently, obtaining reliable mass estimates for SMBHs beyond the local population through dynamical modeling of stellar or gaseous components is not feasible, so scaling relations are used instead.

Black hole mass estimates can be obtained by employing scaling relationships between $M_{\rm BH}$ and the properties of the host galaxy's bulge (P. Salucci et al. 1999; E. Tundo et al. 2007). Additionally, black hole mass can be estimated using the luminosity and width of broad emission lines in AGNs (A. Wandel et al. 1999; M. Vestergaard & B. M. Peterson 2006), as well as their X-ray variability (M. Nikolajuk et al. 2004; X.-L. Zhou et al. 2010; B. C. Kelly et al. 2011). These mass estimates would in turn yield statistically significant samples necessary to determine the BHMF. Comparing BHMFs derived from different black hole mass estimation methods is important to highlight the level of agreement or disagreement between them. Additionally, BHMFs derived from physical models can help determine the primary mechanisms driving black hole growth.

Both *empirical* and *physics-based* models have been used to investigate the multivariate distributions of properties of SMBHs, host galaxies, and their parent halos. We refer to these as *empirical* models, i.e., those that attempt to constrain the connection between dark matter halos and galaxies by assigning galaxies to halos using diverse techniques such as abundance matching (P. Colín et al. 1999); halo occupation distributions (A. V. Kravtsov et al. 2004); conditional luminosity functions (X. Yang et al. 2003), and models that flexibly link galaxies to dark matter halo growth histories over time (C. Conroy & R. H. Wechsler 2009; B. P. Moster et al. 2010; A. P. Hearin & D. F. Watson 2013; R. H. Wechsler & J. L. Tinker 2018; P. Behroozi et al. 2019; H. Zhang et al. 2023). We use the term *physics-based* models to refer to those that evolve galaxies and gas, incorporating an explicit parameterization of the physics involved in galaxy formation. *Physics-based* models can be categorized into *semianalytic* models (SAMs; e.g., R. S. Somerville et al. 2001, 2008, 2015; D. J. Croton et al. 2006, 2016; A. J. Benson 2012; M. B. Henriques et al. 2015; B. R. S. Somerville & R. Davé 2015; A. R. H. Stevens et al. 2016; A. Ricarte & P. Natarajan 2018), and *numerical hydrodynamics* simulations (e.g., N. Khandai et al. 2015; S. McAlpine et al. 2016; T. Naab & J. P. Ostriker 2017; J. P. Naiman et al. 2018). Semianalytic models use prescriptions motivated by observed trends to make physical predictions and track flows between different reservoirs. Numerical simulations solve partial differential equations for hydrodynamics, thermodynamics, and gravity, while self-consistently evolving galaxies alongside the large-scale structure in simulated boxes. Although SAMs and numerical hydrodynamics simulations incorporate black hole growth prescriptions, both explicitly rely on the observationally determined local $M_{\rm BH}$–σ or $M_{\rm BH}$–$M_{\rm bulge}$ relations for calibration. These models contain a diverse set of black hole growth channels that can effectively reproduce observed local black hole scaling relations (R. S. Somerville & R. Davé 2015; M. Habouzit et al. 2022a).

There is considerable disagreement among different large-scale numerical hydrodynamics models about how SMBHs grow as a function of redshift and stellar or halo mass (e.g., P. Natarajan et al. 2023; M. Habouzit et al. 2022a; S. Dattathri et al. 2024). First, the spatial and particle resolution are insufficient to resolve black hole accretion disks. In these models, black hole seeds, growth, and feedback are handled using subgrid physics. Models vary in their subgrid implementations, including the location, mass, and dynamics of black hole seeds, methods for modeling black hole accretion, and different approaches and efficiencies for injecting AGN energy and releasing it. Some simulations explicitly link AGN feedback channels to black hole mass, while others assume a uniform feedback mechanism. For a more comprehensive comparison between numerical hydrodynamics models, please see Table 1 from M. Habouzit et al. (2022b).

In this work, we look at the properties of black hole populations and how they evolve over time for DARK SAGE, RICARTE & NATARAJAN's SAM, the SANTA CRUZ SAM, the TRINITY empirical model, and the ILLUSTRISTNG300 simulation. Then, we focus on deriving predictions for SMBH mass assembly histories from DARK SAGE. We parse the DARK SAGE black hole mass growth channels over cosmic time and quantify the relative contribution of accretion processes versus mergers. Our goal is to understand the physical processes responsible for SMBH growth. In particular, how do physics-based models compare with observations, and what are the growth channels responsible for the bulk of black hole growth?

This paper is organized as follows. In Section 2, we present an overview of the models used in this paper. Section 3 compares black hole population properties between DARK SAGE, the SANTA CRUZ SAM, RN18, ILLUSTRISTNG, and TRINITY. In Section 4, we focus on the black hole mass assembly in DARK SAGE through its various physical implementations of black hole growth. We present the discussion and conclusions of this study in Section 5. Appendix A provides more details about model calibration methods. Appendix B includes the Eddington ratio distributions divided into halo mass bins for DARK SAGE, the SANTA CRUZ SAM, RN18, and ILLUSTRISTNG.

2. Black Hole Growth Models

In this section, we briefly summarize black hole seeding and growth prescriptions adopted in DARK SAGE, RN18, the SANTA CRUZ SAM, ILLUSTRISTNG, and TRINITY. Section 2.1 describes the DARK SAGE semianalytic model. Sections 2.2 and 2.3 present a brief summary of the RN18 models and the SANTA CRUZ SAM, respectively. In Section 2.4, we summarize the numerical hydrodynamics simulation ILLUSTRISTNG300-1, and in Section 2.5, we describe the semiempirical model TRINITY. Table 1 provides a summary of the details of the models used in our analysis. Note that the minimum halo mass in the models using *N*-body simulations assumes that each halo contains at least 200 particles at $z = 0$.

2.1. Semianalytic Model: DARK SAGE

DARK SAGE (A. R. H. Stevens et al. 2016) is a semianalytic model of galaxy formation that couples empirical and phenomenological analytic prescriptions to describe the underlying physics of galaxy formation and evolution. This framework takes as an input a set of dark matter merger trees from the Millennium *N*-body simulation (V. Springel et al. 2005) and populates it with the predetermined physical conditions. The simulation uses a periodic box of length 684.9 Mpc with particle mass resolution of $1.1 \times 10^9 M_\odot$ and cosmological parameters from the Wilkinson Microwave Anisotropy Probe data (D. N. Spergel et al. 2003), where $\Omega_M = 0.25$, $\Omega_\Lambda = 0.75$,

Table 1
Summary of Details Pertaining to Black Hole Properties from Our Model Comparisons in Figure 3

Model Name	Model Type	Minimum Halo Mass ($M_\odot$)	Black Hole Seeding
DARK SAGE	SAM	$10^{11.2}$	$0\ M_\odot$
RN18	SAM	5×10^6	Light (common): $30\ M_\odot \leqslant M_\bullet \leqslant 100\ M_\odot$. Heavy (rare): $\sim 10^5\ M_\odot$
SANTA CRUZ	SAM	10^{10}	$\sim 10^4\ M_\odot$
TNG300-1	Hydro sim	10^{10}	$1.1 \times 10^6\ M_\odot$
TRINITY	Empirical	10^{11}	Functional black hole occupation fraction (see Equation (29) in H. Zhang et al. 2023)

$\Omega_b = 0.045$, $\sigma_8 = 0.9$, and $h = 0.73$. The merger trees are constructed with L-HALOTREE (V. Springel 2005), and the halos and subhalos are found using the SUBFIND algorithm (V. Springel et al. 2001).

DARK SAGE is the predecessor of SAGE (D. J. Croton et al. 2016), in which the modeling starts with hot gas reservoirs modeled as an isothermal sphere within every dark matter halo. Through radiative cooling and condensation of hot gas, galaxies start to form and grow (S. D. M. White & M. J. Rees 1978). As hot gas cools, it collapses gravitationally to form galactic disks (H. J. Mo et al. 1998). DARK SAGE uniquely evolves this one-dimensional disk structure, which is divided into 30 equally spaced logarithmic bins of fixed specific angular momentum. The model uses two separate annular disk structures, one for stars and one for the gas, to allow for convenient computation of relevant physical processes for the two species. DARK SAGE tracks Toomre instabilities (A. Toomre 1964) via a process of redistributing unstable gas or stars to adjacent rings while conserving angular momentum (see J. Binney & S. Tremaine 1987; J. E. Pringle & A. King 2007; A. B. Romeo & J. Wiegert 2011; A. B. Romeo et al. 2023). When a particular ring becomes unstable, it can catalyze a burst of star formation and damp these instabilities. When these instabilities propagate to the innermost ring, unstable stars contribute to the instability-driven bulge, while unstable gas is channeled directly to feed the central black hole. When a galaxy merger occurs, the angular momentum vectors of disks are summed, and misalignment between these vectors results in an overall gain or loss of specific angular momentum.

In DARK SAGE, black hole seeds with zero mass are planted into every well-resolved halo that forms in the Millennium N-body simulation. Thereafter, black holes grow via five main channels:

1. Accretion from hot halo gas, referred to as the hot mode;
2. Cold gas accretion from galaxy mergers, referred to as the cold mode;
3. Ex situ gas accretion from unstable cold gas with low angular momentum driven by galaxy mergers, referred to as the merger-driven instability;
4. In situ gas accretion from unstable cold gas with low angular momentum, referred to as the secular instability; and
5. Mergers with other black holes (BH–BH merger mode).

We now describe each of these pathways in more detail. During major galaxy mergers (i.e., when the baryonic-mass ratio[7] of the merging galaxies is >0.3), the two black hole masses are simply summed together, yielding the BH–BH merger mass growth channel. No black hole dynamics is implemented for black hole merger growth. Due to the absence of implementation of an explicit dynamical friction model, the mass produced from BH–BH mergers can be considered an upper limit to what a more realistic contribution from this channel might be as mergers might take a finite time and not always lead to completion. As galaxies evolve, black holes accumulate mass through cold gas accretion or secular instabilities, which occurs as a result of the Toomre disk instabilities noted above and galaxy mergers. This mode may be episodically dependent on the in situ cold gas availability, merger rate of galaxies, and their star formation history. In the case of hot-mode gas accretion, it involves direct funneling of gas from the circumgalactic medium (CGM) or the intrahalo medium. The accretion of gas from the hot halo is modeled using the Bondi–Hoyle–Lyttleton formula (H. Bondi 1952). In the case of cold-mode accretion, when a merger occurs, as described above, a fraction of gas denoted as $f_{\rm BH}$ is used to directly feed the central black hole on short timescales, which results in rapid black hole growth following Equation (1), adapted from G. Kauffmann & M. Haehnelt (2000). This is applied individually to each annulus:

$$\Delta m_{\rm cold} = f_{\rm BH}\left[1 + \left(\frac{280\ {\rm km\ s^{-1}}}{V_{\rm vir}}\right)^2\right]^{-1} \times \sum_{i=1}^{30}(m_{\rm i,cen} + m_{\rm i,sat})\min\left(\frac{m_{\rm i,sat}}{m_{\rm i,cen}}, \frac{m_{\rm i,cen}}{m_{\rm i,sat}}\right). \qquad (1)$$

The quantity $\Delta m_{\rm cold}$ represents the cold gas mass that is fed into the black hole from the disk. The parameter $f_{\rm BH}$ determines the efficiency of this accretion process and governs the proportion of cold gas intake attributed to major and minor mergers. Currently, the DARK SAGE fiducial model sets $f_{\rm BH} = 20\%$. We discuss the implications of our results when lowering this value in Section 5. Additionally, $m_{\rm i}$ denotes the gas mass within the ith annular region, whether it pertains to the central galaxy or a satellite galaxy. It is worth noting that the majority of the gas that black holes accrete has low specific angular momentum, akin to what is commonly observed in N. N. Sanchez et al. (2018).

When a major galaxy merger occurs, after gas is funneled directly into the central black hole, the residual gas ($1 - f_{\rm BH}$) from the secondary galaxy is added to the primary's disk. Thereafter, each annulus is subject to a merger-driven starburst phase following the prescription in R. S. Somerville et al. (2001). Any remaining cold gas that exhibits gravitational instability undergoes the standard procedure implemented in DARK SAGE, which was briefly outlined in the preceding section, for the fate of unstable gas. The redistribution of this unstable gas might incite instabilities in other regions of the disk, potentially leading to a chain reaction that persists until the unstable gas reaches the innermost annulus. At this stage, a

---

[7] The baryonic-mass ratio does not include the hot gas and intracluster stars.

fraction of the inflowing gas is funneled directly onto the black hole. We refer to this accreted component as the merger-driven instability channel. We note that DARK SAGE limits the hot-mode accretion to the Eddington limit. No other black hole growth channel follows such restrictions; therefore, super-Eddington accretion is permitted for the other growth modes.

In this paper, we use the 2018 version of DARK SAGE (A. R. H. Stevens et al. 2018). In this version, DARK SAGE updates the way in which the cooling scale radius and the velocity dispersion support in disks are calculated. Although a new version of DARK SAGE is now public (A. R. H. Stevens et al. 2024), for more information about our specific version, see A. R. H. Stevens et al. (2016).

2.2. The Semianalytic Model of RN18

Another SAM that we compare within this work is the RN18 model, which employs a different set of recipes for BH seeding, growth, and feedback. The RN18 model takes a hybrid empirical and analytic approach to model the growth of SMBHs from $z = 20$ to $z = 0$ deeply embedded in the cold dark matter paradigm. The RN18 model uses Planck Collaboration et al. (2016) cosmological parameters. Analytic dark matter merger trees generated using the H. Parkinson et al. (2008) algorithm (based on the formalism of W. H. Press & P. Schechter 1974) form the backbone of the model. This technique has the advantage of enabling a much higher dynamic range than N-body based merger trees (down to a minimum halo mass of $5 \times 10^6\,M_\odot$ in these models) at the cost of spatial information. RN18 assumes empirical relationships between galaxies and their host dark matter halos, then models SMBH–galaxy coevolution semianalytically. The model does not directly track gas evolution and star formation, instead relying on only one property: the galaxy's stellar velocity dispersion σ, which is estimated from the stellar mass and size (see Figure 4 of RN18). Recent James Webb Space Telescope (JWST) data indicate that the local $M_\bullet$–σ relation appears to hold even for samples at $4 \lesssim z \lesssim 11$ although the $M_\bullet$–M_* relation arguably varies with redshift (R. Maiolino et al. 2023).

The RN18 model includes several variations that explore different physical assumptions.

1. *Seeding.* First, SMBHs are initialized as either "light" or "heavy" seeds in the redshift range $15 \leqslant z \leqslant 20$. Light seeds are assumed to be common but low mass ($30\ M_\odot \leqslant M_\bullet \leqslant 100\ M_\odot$), while heavy seeds are rare but high mass ($\sim 10^5\,M_\odot$ following the formalism of G. Lodato & P. Natarajan 2006, 2007, which is based solely on dark matter halo mass, redshift, and angular momentum, neglecting the radiation field).
2. *Growth.* When a major halo merger (mass ratio of 1:10 or greater) occurs, SMBHs grow via the "burst" mode at the Eddington limit until they reach the $M_\bullet$–σ relation. If they are not growing in this mode, they instead grow through a "steady" mode. In the "power-law" models included in this paper, a universal Eddington ratio distribution function is assumed, which is subdominant in terms of SMBH growth, but important for reproducing observed luminosity functions.
3. *Dynamics.* When a major halo merger occurs, SMBHs may merge with probability $p_{\rm merge}$ at the same time the burst mode is triggered, after a dynamical friction time delay estimated by the M. Boylan-Kolchin et al. (2008) formulae. No further black hole dynamics modeling is implemented after the galaxies merge. RN18 found that models with $p_{\rm merge} = 1$ would overshoot the local $M_\bullet$–σ relationship because SMBH–SMBH mergers become the dominant growth mode in the most-massive halos.

2.3. The SANTA CRUZ Semianalytic Model

The SANTA CRUZ SAM (R. S. Somerville & J. R. Primack 1999; R. S. Somerville et al. 2001, 2008, 2015; L. A. Porter et al. 2014) is based within the backbone of cosmological merger trees, and uses simple, physically motivated recipes to track the flows of gas from the intergalactic medium (IGM) into the CGM and then into the interstellar medium (ISM), where it can form stars. Massive stars and supernovae drive outflows that eject gas from the ISM, back into the CGM and IGM. Cold ISM gas is partitioned into different phases (atomic, molecular, and ionized) using a prescription based on hydrodynamic simulations, and the transformation of molecular gas into stars is modeled using an empirical relationship based on observations of nearby galaxies (R. S. Somerville et al. 2015). The model predicts a wide range of galaxy properties over cosmic time, like stellar mass, SFR, and the metallicity of gas and stellar phases, and has been used extensively to create forecasts and mock catalogs for comparison with past, present, and future astronomical surveys (R. S. Somerville et al. 2021; L. Y. A. Yung et al. 2022, 2023). These works and others have shown that the SANTA CRUZ SAM reproduces many key observational constraints on galaxy properties from $0 \lesssim z \lesssim 10$.

In the SANTA CRUZ model, each dark matter halo with no progenitor is seeded with a black hole of fixed mass, typically $\sim 10^4\,M_\odot$ (R. S. Somerville et al. 2008; M. Hirschmann et al. 2012). Black holes grow through Bondi accretion of gas from the hot halo, and inflows of cold gas from the ISM, driven either by internal gravitational instabilities or mergers triggering the radiatively efficient mode (which is analogous to the cold mode). Similar to DARK SAGE, the SANTA CRUZ SAM provides a channel for bulge and black hole growth through disk instabilities. The main difference between DARK SAGE and the SANTA CRUZ SAM in this regard is the details of how the instabilities are calculated. The SANTA CRUZ SAM employs a metric from G. Efstathiou et al. (1982) to determine when disks become unstable. Using N-body simulations, G. Efstathiou et al. (1982) showed that disks become unstable when the ratio between dark matter mass and disk mass drops below a specific threshold. They provide a parameterization defining the initiation of disk instabilities as follows:

$$M_{\rm disk,crit} = \frac{v_{\rm max}^2\, R_{\rm disk}}{G \quad \epsilon}, \tag{2}$$

where $M_{\rm disk,crit}$ represents the threshold disk mass, beyond which the disk is expected to become unstable. $v_{\rm max}$ denotes the peak circular velocity, $R_{\rm disk}$ stands for the exponential disk scale length, and ϵ is the stability parameter. Here, the SANTA CRUZ SAM uses an $\epsilon = 0.75$.

For disk-instability triggered black hole growth, the SANTA CRUZ SAM assumes a constant Eddington ratio of $f_{\rm edd} = 0.01$ with a Gaussian distributed scatter of 0.02 dex, motivated by observations (M. Hirschmann et al. 2012). Black holes continue to accrete as long as there is remaining gas fuel in the “bulge reservoir,” with the accretion rate given by:

$$\dot{M}_{\bullet,\mathrm{disk}} = 1.26 \times 10^{38}\ \mathrm{erg\ s^{-1}}\ \frac{1-\epsilon}{\epsilon}\frac{f_{\mathrm{edd}}}{c^2}M_{\bullet}. \tag{3}$$

The model also includes rapid black hole growth via gas accretion triggered by galaxy–galaxy mergers, based on findings from cosmological binary merger simulations (P. F. Hopkins et al. 2005b; T. J. Cox et al. 2006, 2008; B. Robertson et al. 2006). During this phase, the black hole accretes matter at the Eddington rate until it reaches a critical mass, at which point the energy emitted becomes sufficient to stop further accretion. Following this, the accretion rate gradually decreases in a power-law “blow-out” phase until the black hole bright mode is turned off (P. F. Hopkins et al. 2005a). For further details, refer to R. S. Somerville et al. (2008) and M. Hirschmann et al. (2012). Additional model updates are described in L. Y. A. Yung et al. (2021).

The Santa Cruz SAM estimates the merger rates of satellite galaxies within their host dark matter halos using the modified Chandrasekhar formula of M. Boylan-Kolchin et al. (2008), as described in detail in R. S. Somerville et al. (2008). The SMBH within each galaxy are assumed to merge instantaneously when the galaxies merge, with the sum of the SMBH remnant being equal to the sum of the progenitor masses.

We use central and satellite galaxies only from the SANTA CRUZ SAM. In this study, we use the version of the SANTA CRUZ SAM recently presented by A. Gabrielpillai et al. (2022, 2025 in preparation). Here, the SAM is run within dark matter merger trees generated using the ROCKSTAR halo finder (P. S. Behroozi et al. 2013a) and CONSISTENT-TREES merger tree codes (P. S. Behroozi et al. 2013b) run on the ILLUSTRISTNG 300-1 dark-matter-only simulation (more on ILLUSTRISTNG are provided below in Section 2.4). The cosmological parameters adopted in this run of the SANTA CRUZ SAM are the same as those adopted by ILLUSTRISTNG, and are consistent with Planck results (Planck Collaboration et al. 2016). The values of the free parameters in the SAM have been adjusted slightly relative to previous work to account for the change in the merger trees (see A. Gabrielpillai et al. 2022 for details).

2.4. The *ILLUSTRISTNG300-1* Simulation

The Next Generation ILLUSTRIS simulations (ILLUSTRISTNG) come in a suite of numerical hydrodynamics simulations with subgrid prescriptions for SMBH evolution and star formation (F. Marinacci et al. 2018; J. P. Naiman et al. 2018; D. Nelson et al. 2018, 2019; A. Pillepich et al. 2018; V. Springel et al. 2018). This simulation is an upgraded version derived from the original ILLUSTRIS model (S. Genel et al. 2014; M. Vogelsberger et al. 2014a, 2014b; D. Nelson et al. 2015; D. Sijacki et al. 2015), incorporating a comprehensive array of physical mechanisms including gas dynamics processes like cooling and heating, star formation, feedback from stars, black hole growth, and the feedback from AGNs. Analysis of simulation slices have been used to examine the impact of feedback mechanisms in shaping galactic properties (R. Weinberger et al. 2018; B. A. Terrazas et al. 2020), establishing links between galaxy properties and the dark matter halos enveloping them (S. Bose et al. 2019; D. Martizzi et al. 2020; L. Zanisi et al. 2020), exploring the traits of galaxy clusters and their constituent galaxies (M. Ntampaka et al. 2019; G. D. Joshi et al. 2020; L. V. Sales et al. 2020), and predicting high-redshift JWST results (X. Shen et al. 2020b, 2022b; M. Vogelsberger et al. 2020).

There are three main boxes in the suite with side lengths of approximately 50, 100, and 300 cMpc, tracing the formation and evolution of structures influenced by gravity and magnetohydrodynamics, spanning from the Universe’s early stages to $z = 0$. In this paper, we compare our SAMs to the 300 cMpc box with highest resolution (the TNG300-1 is referred hereafter to as TNG300-1), which has a particle mass resolution of $5.9 \times 10^7\,M_{\odot}$ and uses cosmological parameters derived from Planck (Planck Collaboration et al. 2016), specifically $\Omega_M = 0.3089$, $\Omega_\Lambda = 0.6911$, $\Omega_b = 0.0486$, and $h = 0.6774$. As stated before, We use central and satellite galaxies in our sample. For the purpose of our comparison, we note that both TNG300-1 and Millennium (which is used to run DARK SAGE) use Friends-of-Friends (FoF) and SUBFIND. We consistently use $M_{200\mathrm{crit}}$, which is the total mass in the FoF halo enclosed in a sphere whose mean density is 200 times the critical density of the Universe at the time the halo is recorded to set halo masses.

In TNG300-1, black holes with a mass of $1.1 \times 10^6\,M_{\odot}$ are seeded in every halo that reaches a mass of $7 \times 10^{10}\,M_{\odot}$ (R. Weinberger et al. 2017). Soon after being seeded, these black holes start growing through Bondi accretion (Equation (4)) capped at the Eddington rate (Equation (5)). The resulting accretion rate is determined by the lesser of the two rates, denoted as $\dot{m}_{\mathrm{BH}}$ in Equation (6),

$$\dot{m}_{\mathrm{Bondi}} = \frac{4\pi G^2 m_{\mathrm{BH}}^2 \rho}{c_s^3}, \tag{4}$$

$$\dot{m}_{\mathrm{Edd}} = \frac{4\pi G m_{\mathrm{BH}} m_p}{\epsilon_r \sigma_T}\quad c, \tag{5}$$

$$\dot{m}_{\mathrm{BH}} = \min(\dot{m}_{\mathrm{Bondi}},\ \dot{m}_{\mathrm{Edd}}), \tag{6}$$

where c_s is the speed of sound of the local ISM, ρ is the density of the nearby heated gas, ϵ_r is the efficiency of radiative accretion assumed to be 0.2, and σ_T is the Thompson cross section.

Once Equation (6) is calculated, one can determine if the black hole accretion comes from the thermal mode or kinetic mode. To determine which TNG300-1 black holes accrete in each of these modes, a black hole mass-dependent threshold is applied using the following equation:

$$\chi = \min\left[0.002\left(\frac{M_{\mathrm{BH}}}{10^8\,M_{\odot}}\right)^2, 0.1\right]. \tag{7}$$

If the Eddington ratio exceeds this threshold, the black hole is deemed to be accreting in the thermal mode, whereas if the Eddington ratio is lower than the threshold, the black hole grows through kinetic-mode accretion. Other than these two modes, black holes may also grow by merging with other black holes when galaxies merge. As in DARK SAGE and the SANTA CRUZ SAM, no black hole dynamics are included in the simulation. Once merged and at any point in the history of the halo that hosts a black hole, the model enforces the SMBH position to be at the potential minimum of its host halo at every global integration time step (R. Weinberger et al. 2018).

2.5. The *TRINITY* Empirical Model

TRINITY connects galaxy properties to SMBHs (H. Zhang et al. 2023) using the UNIVERSEMACHINE (P. Behroozi et al. 2019) machinery as its foundation. First, the model defines the galactic star formation rate (SFR) as a function that depends both on the halo mass and redshift. Within this parameter space, considering the average mass growth history of halos, an integration of the resulting SFRs is performed. TRINITY is constructed to reproduce the observed stellar mass functions (SMFs), galaxy quenched fractions, cosmic SFRs, specific SFRs, galaxy UV luminosities, quasar luminosity functions, quasar probability distribution function, active SMBH mass function, SMBH mass–bulge mass relation, and the SMBH mass distribution of bright quasars within $z = 0$–10. TRINITY has the largest number of free parameters of the models in our study (56; see Appendix A). As a result, the model outputs a stellar mass-to-halo mass relation. This calculated stellar mass is used to obtain bulge masses using observational scaling relations (N. Häring & H.-W. Rix 2004; A. Beifiori et al. 2012; J. Kormendy & L. C. Ho 2013; N. J. McConnell & C.-P. Ma 2013; G. A. D. Savorgnan et al. 2016). The chosen SMBH mass–bulge mass relation determines the average accretion rates of SMBHs, because the growth history of galaxies on average is determined by the relationship between SFR and halo mass. The distributions of Eddington ratios and the radiative efficiency are parameterized, and they dictate how the growth of SMBHs is connected to the observed distribution of SMBH luminosities. Lastly, the model compares these predictions to calculate a likelihood function and employs a Markov Chain Monte Carlo (MCMC) algorithm to derive the posterior distribution of model parameters that align with the observed data. Like TNG300-1, TRINITY uses a flat Λ cold dark matter cosmology consistent with Planck results (Planck Collaboration et al. 2016).

3. Comparison of Models: A Diversity of SMBH Assembly Histories

In this section, we present the results of comparing empirical, semianalytic models, and numerical hydrodynamics simulations. Section 3.1 discusses the local BHMF. The evolution of black hole mass is highlighted in Section 3.2. Section 3.3 shows the time evolution of the Eddington ratio distributions. Lastly, Section 3.4 compares the predicted and observationally inferred cosmic SMBH mass density functions.

3.1. Local Black Hole Mass Function

The SMBH mass function offers a valuable overview of the statistics of the local population of black holes. The inferred BHMF varies significantly depending on the choice of SMF, black hole mass scaling relation, or AGN accretion history. The top panels of Figure 1 compare the SMF and black hole mass–stellar mass relation at $z = 0$. While I. K. Baldry et al. (2008) and M. Bernardi et al. (2013) agree up to $M_* \sim 10^{11}\,M_\odot$, the latter predicts a higher number density at larger masses. As a result, models calibrated to M. Bernardi et al. (2013), such as the SANTA CRUZ SAM and TNG300-1, produce a higher number density of massive galaxies. In contrast, TRINITY and RN18 rely on SMFs from I. K. Baldry et al. (2012), J. Moustakas et al. (2013), and B. P. Moster et al. (2013), which are more consistent with I. K. Baldry et al. (2008).

Studies have shown that the number density of massive galaxies has been underestimated by factors of 3–10 for $M_* \sim 10^{11-11.6}\,M_\odot$ and by up to 100 times for even higher stellar masses (M. Bernardi et al. 2017a, 2017b). M. Bernardi et al. (2018) suggested that a varying initial mass function (likely bottom-heavy in the most-massive galaxies with high velocity dispersion) implies a larger quantity of massive galaxies than predicted by the Santa Cruz SAM. Therefore, models calibrated to I. K. Baldry et al. (2008), I. K. Baldry et al. (2012), and J. Moustakas et al. (2013) likely underestimate the number of massive black holes, affecting even the D. W. Pesce et al. (2021) "upper limit" based on the UNIVERSEMACHINE, which uses the SMF from J. Moustakas et al. (2013). Unless scaling relations become steeper at high masses, their inferred BHMFs likely underrepresent the high-mass end. Older empirical models based on pre–Sloan Digital Sky Survey (SDSS) or early data release eargalaxy mass functions and velocity dispersion functions have been superseded.

For the black hole mass–stellar mass relation, we see overlap between the SANTA CRUZ SAM and RN18 models (solid green line: $p_{\rm merge} = 0.1$, solid light-green line: $p_{\rm merge} = 1.0$). DARK SAGE and TNG300-1 closely follow each other's mean relation for $M_{\rm BH} > 10^{10.2}\,M_\odot$. All of our physics-based models fall within J. E. Greene et al. (2020) and A. E. Reines & M. Volonteri (2015) observations. For $M_{\rm BH} > 10^{11}\,M_\odot$, even though both the SANTA CRUZ SAM and TNG300-1 are calibrated to match M. Bernardi et al. (2013), they have different $M_{\rm BH}$–M_* normalizations. This is because the SANTA CRUZ SAM is tuned to match the local black hole mass–bulge mass relation from N. J. McConnell & C.-P. Ma (2013). The local black hole mass–bulge mass relation in DARK SAGE has a lower normalization, leading to a shallower $M_{\rm BH}$–M_* relation. Interestingly, the SANTA CRUZ SAM and the RN18 $p_{\rm merge} = 1.0$ model converge at high masses, despite the latter not modeling bulges. This suggests that a higher black hole merger rate could also raise the normalization of the $M_{\rm BH}$–M_* relation.

The normalization of the black hole mass–bulge mass relation varies by a factor of 2–3 (J. Kormendy & L. C. Ho 2013), with more recent estimates favoring higher black hole-to-bulge mass ratios at the high-mass end. For example, TRINITY uses datasets that equally weight older samples like N. Häring & H.-W. Rix (2004), which report a lower normalization, compared to newer scaling relations like those in J. Kormendy & L. C. Ho (2013). ETHER+WISE use a modified version of Z. Schutte et al. (2019), which has a comparable black hole mass–bulge mass normalization to J. Kormendy & L. C. Ho (2013). There is a general agreement that the normalization of these scaling relations is on the higher side, which in turn leads to a more prominent BHMF at the massive end.

The bottom two panels show the local BHMFs for observations (left) and the physics-based models (right). In general, observations agree within $\lesssim$0.8 dex for $M_{\rm BH} \sim 10^{7-8}\,M_\odot$ SMBHs. For $M_{\rm BH} < 10^7\,M_\odot$, the differences between the observations increase to $\lesssim$1.5 dex. By $M_{\rm BH} \sim 10^{10}\,M_\odot$, we show the largest disagreement between the observations, with a scatter of $\lesssim$4.6 dex. First, A. Merloni & S. Heinz (2008) derived the BHMF by converting AGN X-ray luminosity to black hole accretion rates, which depend on the Eddington ratio, and applying the continuity equation (A. Cavaliere et al. 1971; T. A. Small & R. D. Blandford 1992). While their results align with the TRINITY model, uncertainties remain, particularly in the bolometric correction of the local BHMF. Their method primarily accounts for low-accretion rate objects ($L/L_{\rm edd} < 10^{-2}$) and extrapolates to higher rates under the assumption that radio

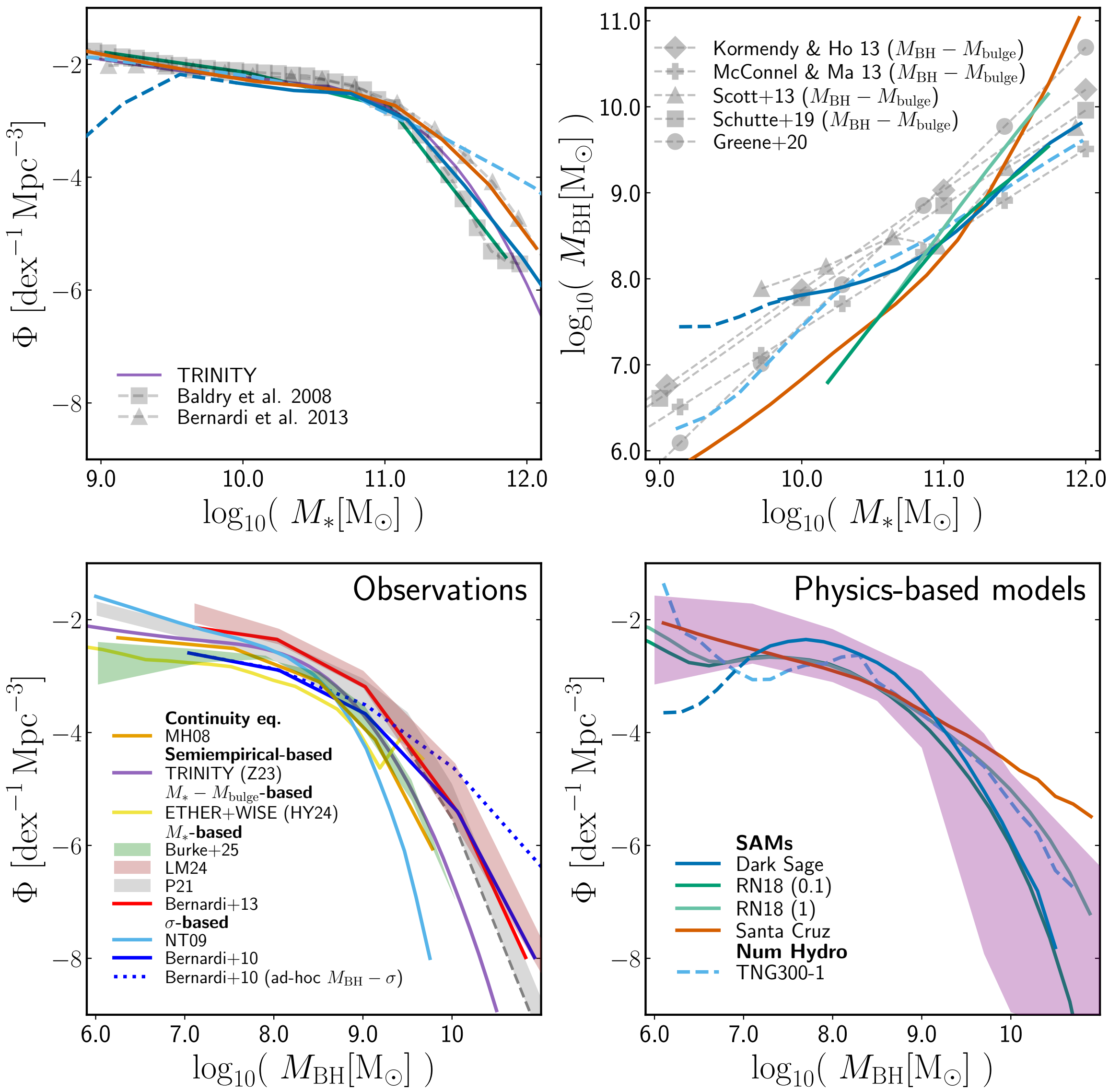

Figure 1. The stellar mass function, black hole mass–stellar mass relation, and the black hole mass function (BHMF) at $z = 0$. The top-left panel shows the semianalytic models DARK SAGE (solid dark-blue line), the SANTA CRUZ SAM (solid brown line), and RN18 (solid green line: $p_{\rm merge} = 0.1$, solid light-green line: $p_{\rm merge} = 1$). We include TRINITY (solid purple line) and TNG300-1 (dashed cyan line). The observed SMF from I. K. Baldry et al. (2008) and M. Bernardi et al. (2013; used to calibrate DARK SAGE, the SANTA CRUZ SAM, and TNG300-1) are included, while RN18 models use the stellar mass function from B. P. Moster et al. (2013). The top-right panel presents the mean of these models alongside observational data from J. E. Greene et al. (2020) and A. E. Reines & M. Volonteri (2015). The bottom-left panel categorizes observational constraints based on inferred BHMFs, showing: the continuity equation from A. Merloni & S. Heinz (2008; solid orange line), semiempirical methods from H. Zhang et al. (2023), stellar mass–bulge mass relation from V. Ramakrishnan et al. (2023) and J. Hernández-Yévenes et al. (2024; ETHER+WISE shown in solid yellow-green line), stellar mass constraints from C. J. Burke et al. (2025), E. R. Liepold & C.-P. Ma (2024), D. W. Pesce et al. (2021), and M. Bernardi et al. (2013; shown as green, dark-red, and gray shaded regions, and the solid red line, respectively), and the velocity dispersion function from P. Natarajan & E. Treister (2009; solid light-blue line), M. Bernardi et al. (2010; solid blue line), and the $M_{\rm BH}$–σ scaling relation from G. Sato-Polito et al. (2023) with M. Bernardi et al. (2010). The bottom-right panel compares our physics-based models, with the violet shaded area representing the range of observational results from the bottom-left panel. Note that the dashed line for DARK SAGE represents galaxies in halos with fewer than 200 particles. The gray dashed line in the bottom-left panel from D. W. Pesce et al. (2021) denotes extrapolated BHMFs for $M_{\rm BH} > 10^{9.5}\ M_\odot$. Our results for the SANTA CRUZ SAM on TNG300 dark matter trees are consistent with A. Gabrielpillai et al. (2022), who used the SANTA CRUZ SAM model on dark matter trees from the TNG100 simulation. We find significant discrepancies in the observed BHMF. The physics-based models fall within the observed range.

luminosity is weak in the radiatively efficient mode. However, AGNs in this mode significantly contribute to the X-ray luminosity function. For this reason, there is potential for substantial systematic errors in their BHMF estimate.

The TRINITY model may decline exponentially at the high-mass end because it relies on the SMF from I. K. Baldry et al. (2012) and J. Moustakas et al. (2013), along with their relatively shallow $M_{\rm BH}$–M_* and $M_{\rm BH}$–$M_{\rm bulge}$ relations in this regime. For the bulge mass–stellar mass-inferred BHMF, we include the Event Horizon and Environs (ETHER) catalog, which currently compiles 3.15 million black hole mass estimates, approximately 20,000 mas-scale radio fluxes, around 36,000 hard X-ray fluxes, and spectral energy distribution information derived from existing catalogs, database queries, and literature (V. Ramakrishnan et al. 2023; J. Hernández-Yévenes et al. 2024; D. G. Nair et al. 2024). This is combined with the Wide-field Infrared Survey Explorer (WISE) catalog, a comprehensive database with infrared wavelengths at 3.4 μm, 4.6 μm, 12 μm, and 22 μm collected by WISE (E. L. Wright et al. 2010). J. Hernández-Yévenes et al. (2024) estimated stellar masses and bulge fractions using WISE photometry, calibrated to the Galaxy and Mass Assembly (GAMA) optical survey (S. P. Driver et al. 2011). They adopted a modified Z. Schutte et al. (2019) black hole mass–bulge mass relation, which is closely aligned with J. Kormendy & L. C. Ho (2013). We see that between $M_{\rm BH} \sim 10^{7-9}\,M_\odot$ ETHER+WISE show the lowest number density of all observational samples. Above this range, there is a raise in the number density that comes from not considering the intrinsic scatter of the black hole mass–bulge mass relation (J. Hernández-Yévenes et al. 2024). At the high-mass end, ETHER+WISE agree with M. Bernardi et al. (2013), D. W. Pesce et al. (2021), and E. R. Liepold & C.-P. Ma (2024).

C. J. Burke et al. (2025) developed a Bayesian model to infer the BHMF by analyzing X-ray, radio, and optical variability observations. Here, they use the data release 4 of the GAMA survey (S. P. Driver et al. 2022), convolved with the $M_{\rm BH}$–M_* relations from J. E. Greene et al. (2020). Below $M_{\rm BH} < 10^9\,M_\odot$, C. J. Burke et al. (2025) is consistent with the ETHER+WISE sample, which agrees with results from tidal disruption event estimates (Y. Yao et al. 2023). At the lowest black hole masses, A. Merloni & S. Heinz (2008), TRINITY, D. W. Pesce et al. (2021), and P. Natarajan & E. Treister (2009) predict a number density roughly an order of magnitude higher than that of C. J. Burke et al. (2025). Above $M_{\rm BH} > 10^9\,M_\odot$, C. J. Burke et al. (2025), A. Merloni & S. Heinz (2008), and TRINITY converge, while D. W. Pesce et al. (2021) and E. R. Liepold & C.-P. Ma (2024) lie with a higher number density at roughly all masses. The SMF used in E. R. Liepold & C.-P. Ma (2024) includes the results of the MASSIVE survey (C.-P. Ma et al. 2014; M. Gu et al. 2022; for $M_* > 10^{11.5}\,M_\odot$) and J. Leja et al. (2020; for $M_* < 10^{11.3}\,M_\odot$), with an assumed $M_{\rm BH}$–M_* relation from J. Kormendy & L. C. Ho (2013). Between $M_{\rm BH} \sim 10^{8-10.2}\,M_\odot$, E. R. Liepold & C.-P. Ma (2024) overlaps with BHMF limits from D. W. Pesce et al. (2021). Outside of this range, E. R. Liepold & C.-P. Ma (2024) is above most observations, with the exception of M. Bernardi et al. (2010) and G. Sato-Polito et al. (2023; ad hoc $M_{\rm BH}$–σ at the high mass end. The BHMF inferred from M. Bernardi et al. (2013) is consistent with E. R. Liepold & C.-P. Ma (2024) shaded region. D. W. Pesce et al. (2021) considered a wide range of possible BHMFs and presents a "lower" and "upper" limit from $z = 0$–6. The "lower" BHMF limit comes from F. Shankar et al. (2009) derived from the continuity equation. The "upper" BHMF limit is inferred empirically using the UNIVERSEMACHINE SMF (P. Behroozi et al. 2019) combined with the black hole mass–stellar mass scaling relation from J. Kormendy & L. C. Ho (2013). It is possible that other black hole mass–stellar mass relations may change this "upper" limit slightly.

P. Natarajan & E. Treister (2009) derived the BHMF using the number density of black holes from SDSS (D. G. York et al. 2000). The BHMF at the high-mass end decreases at $M_{\rm BH} < 10^{10}\,M_\odot$ because, at that time, SDSS had not surveyed as large of a volume as it has in more recent observations. M. Bernardi et al. (2010) used the velocity dispersion function and the $M_{\rm BH}$–σ scaling relation from G. Sato-Polito et al. (2023). M. Bernardi et al. (2010) overlaps with E. R. Liepold & C.-P. Ma (2024) and partially with D. W. Pesce et al. (2021) above $M_{\rm BH} > 3 \times 10^9\,M_\odot$. At lower black hole masses, it shows a lower number density compared to most M_*-based BHMFs. G. Sato-Polito et al. (2023) introduced a steeper second power law in their ad hoc $M_{\rm BH}$–σ relation to match the amplitude of the stochastic gravitational-wave background observed by PTA teams. This BHMF predicts significantly more SMBHs above $M_{\rm BH} > 10^9\,M_\odot$ than a standard single power-law $M_{\rm BH}$–σ relation.

If the high-mass end of the local BHMF is dictated by scaling relations, then tuning the SANTA CRUZ SAM to match both M. Bernardi et al. (2013) and J. Kormendy & L. C. Ho (2013) would likely produce the highest number density of massive black holes among all models. Calibrating to only one of these constraints is not enough. For example, tuning TNG300-1 to M. Bernardi et al. (2013) increases the BHMF by at most $\lesssim$1.3 dex at $M_{\rm BH} \sim 10^{10.5}\,M_\odot$, compared to a model matching the I. K. Baldry et al. (2008) local SMF. Similarly, using a steeper black hole mass–bulge mass relation also results in a $\lesssim$1.3 dex increase in number density at the same mass. Interestingly, E. R. Liepold & C.-P. Ma (2024) derived their stellar mass-inferred BHMF by convolving the SMF with a probability distribution function linked to the $M_{\rm BH}$–M_* relation. They used J. Kormendy & L. C. Ho (2013) and stated that adopting R. P. Saglia et al. (2016) would not significantly alter the results. However, R. P. Saglia et al. (2016) presented a shallower black hole mass–bulge mass relation than J. Kormendy & L. C. Ho (2013), suggesting that steepness alone does not fully explain the high number density of massive black holes.

As seen, the estimates diverge most strongly from each other at the highest and lowest masses. At the lowest masses, number densities are essentially extrapolations from more massive SMBH populations where SMBH–galaxy relationships are known. However, relationships found in high-mass (typically bulge-dominated) galaxies may not all agree for lower-mass galaxies (A. E. Reines & M. Volonteri 2015; M. R. Sturm & A. E. Reines 2024). We find a very large degree of disagreement in the number density of ultramassive black holes (UMBHs), those with $M_{\rm BH} > 10^9\,M_\odot$, which have recently become an observationally exciting mass range due to the detection of the stochastic nHz gravitational-wave background (G. Agazie et al. 2023). At these masses, it has been argued that number densities of UMBHs could plausibly be suppressed due to self-regulated growth imposing, de facto, an upper limit on SMBH masses (P. Natarajan & E. Treister 2009). Recently, several authors have argued that SMBHs in the most-massive galaxies may be systematically over-massive with respect to local scaling relations at lower masses (M. Mezcua et al. 2018; F. Pacucci et al. 2023; M. Mezcua et al. 2024). A larger number density of detected UMBHs than anticipated by most relationships may also help explain the large amplitude of the nHz gravitational-wave background (G. Sato-Polito et al. 2023; D. Izquierdo-Villalba et al. 2024).

In the semianalytic model and numerical hydrodynamics simulation considered in this paper, for $M_{\rm BH} \sim 10^{8-9}\,M_\odot$, all models agree within $\lesssim$0.4 dex. At $M_{\rm BH} \sim 10^{7.1-9}\,M_\odot$, DARK SAGE overpredicts the number of black holes compared to all models. For $M_{\rm BH} < 10^7\,M_\odot$, DARK SAGE predicts a lower number density of BH than the SANTA CRUZ and RN18 SAMs by about 1.3 dex. This difference decreases to 0.7 dex if we remove our DARK SAGE adopted halo mass cut. By $M_{\rm BH} \sim 10^{10}\,M_\odot$, TNG300-1 and the SANTA CRUZ SAM agree in having 0.9 dex higher densities than DARK SAGE and RN18 $p_{\rm merge}$=0.1 model. This difference increases with increasing black hole mass. The SANTA CRUZ SAM and TNG300-1 models are quite similar up to $M_{\rm BH} \sim 10^{10}\,M_\odot$, as demonstrated by A. Gabrielpillai et al. (2022). However, for black holes with masses exceeding $M_{\rm BH} \sim 10^{10}\,M_\odot$, the SANTA CRUZ SAM model predicts a higher number density. Interestingly, the two models from the RN18 SAM, which differ in their predicted probabilities of black hole mergers, provide varying abundances that lie squarely within these mass ranges. The model with the higher black hole merger rate predicts a greater number density of black holes, since SMBH mergers come to dominate the growth of the most-massive SMBHs. Overall, all models fall within the range of observations discussed above.

The discrepancies found in our model comparison can be attributed to differences in calibration procedures (see Appendix A), which in turn rely on observational datasets that often do not agree, and, as we show in later results, the existence of multiple methodologies to derive the same final outcome. Although all of these models are calibrated to match the observed stellar mass function in addition to the $M_{\rm BH}$–σ, $M_{\rm BH}$–M_*, or $M_{\rm BH}$–$M_{\rm bulge}$ relation at $z = 0$, differences in the set of SMF and steepness in the scaling relations used are the most likely cause of the disagreements seen.

3.2. The Evolution of Black Hole Mass

We now turn to the evolution of the SMBH mass function. The BHMF from $z = 0$ to $z = 6$ is plotted in Figure 2. Physics-based models that disagree at $z = 0$ converge between $z \approx 1$–4, with the exception of DARK SAGE, which shows a distinct "knee" near $M_{\rm BH} \sim 10^8\,M_\odot$ that remains fixed across time. This "knee" becomes progressively narrower with increasing redshift, leading to a sharper drop at the high-mass end. We compare our results to A. Merloni & S. Heinz (2008), who used the X-ray AGN luminosity functions and an assumed Eddington ratio distribution. Because they only capture actively accreting black holes, they likely underestimate the number of massive, quiescent black holes. The inferred BHMF from A. Merloni & S. Heinz (2008) comes from the continuity equation, so the mass contribution from SMBH mergers is not taken into account. At $z = 1$, the BHMF from A. Merloni & S. Heinz (2008) is roughly in agreement with most physics-based models. At $z = 2$–3, the disagreement between A. Merloni & S. Heinz (2008) and all models is more apparent at the high-mass end, likely due to sample incompleteness since the lack of non-accreting black holes and SMBH mergers are not included in the inferred BHMF. Interestingly, by $z = 4$, A. Merloni & S. Heinz (2008) closely traced the BHMFs derived from JWST (W. He et al. 2024; J. Matthee et al. 2024; A. J. Taylor et al. 2024). While TNG300-1 and TRINITY align closely with JWST sources at $z = 4$, by $z = 5$, the SANTA CRUZ SAM and RN18 models provide a better match. At $z = 6$, for $M_{\rm BH} > 10^7\,M_\odot$, all models except DARK SAGE underestimate number densities relative to A. J. Taylor et al. (2024).

By construction, the BHMFs from RN18 have an exponential dropoff that becomes steeper with increasing redshift. Both $p_{\rm merge}$ models have consistent BHMFs with each other, except for deviations at the high-mass end below $z < 2$. At fixed mass in this range, the $p_{\rm merge} = 1.0$ model shows a higher number density of black holes than the $p_{\rm merge} = 0.1$ model, indicating a higher rate of BH–BH mergers. Interestingly, by $z = 1$, $p_{\rm merge} = 1.0$ model agrees better with the SANTA CRUZ SAM, while the $p_{\rm merge} = 0.1$ model aligns better with the DARK SAGE prediction.

The SANTA CRUZ SAM aligns closely with RN18, TRINITY, and TNG300-1 between $z = 0$ and 2. Between $z = 3$ and 6, the SANTA CRUZ SAM and TNG300-1 exhibit a sharp drop in number density around $M_{\rm BH} \sim 10^{8-9}\,M_\odot$, likely due to the relatively small volume of the simulation box. By $z = 6$, the SANTA CRUZ SAM and TNG300-1 BHMFs closely agree. In TRINITY, the "knee" in the BHMF becomes less pronounced at higher redshifts. This is because, at high redshift, the M_*–M_h and $M_{\rm BH}$–M_h relationships can be approximated by a single power law (H. Zhang et al. 2023). There is also strong evolution in the BHMF above $z = 5$ driven by universally high Eddington ratios at high redshifts. In fact, TRINITY allows for super-Eddington accretion. In general, the high-growth period ends earlier for more-massive black holes (H. Zhang et al. 2023). This is commonly referred to as "AGN downsizing," whereby more massive active black holes exhibit their peak activity at earlier cosmic epochs (A. Merloni 2004; A. J. Barger et al. 2005; M. Hirschmann et al. 2012). Below $z = 3$, AGN downsizing slows the evolution of the BHMF at the massive end, while $M_{\rm BH} \sim 10^{8-9}\,M_\odot$ grow significantly. This continued growth establishes the "knee" in the BHMF at low redshift. The mild AGN downsizing in DARK SAGE could result from early rapid mass assembly at $z \sim 4$, and sustained accretion of black holes in low-mass halos hosting high stellar mass galaxies likely driven by increased black hole growth via mergers and some cold-mode accretion at $z < 2$.

The number density in the low-mass end in DARK SAGE is underestimated due to the resolution of the underlying dark matter simulation. In general, the BHMF of DARK SAGE stands out as significantly distinct from those of the other models. The magnitude of the bump in DARK SAGE around $M_{\rm BH} \approx 10^8\,M_\odot$ comes from the large contribution of cold-mode accretion during galaxy mergers, that is from ex situ cold gas added directly into the black hole after galaxies merge (see Figure 7). Even if we only account for black holes in $M_h > 10^{12}\,M_\odot$ (dashed–dotted dark-blue line), we see that the bump is preserved with a smaller normalization in the BHMF, indicating both the importance of cold-mode accretion to all black hole masses and the underlying dark-matter-only resolution.

Figure 3 presents the bolometric AGN luminosity function across redshift. We compare predictions from physics-based models to observations from X. Shen et al. (2020a), Y. Harikane et al. (2023), J. E. Greene et al. (2024), J. Guo et al. (2024), R. Maiolino et al. (2024), J. Matthee et al. (2024), H. B. Akins et al. (2024), and V. Kokorev et al. (2024). Note that many of the JWST detected AGN candidates are defined via the existence of a broad component in the Hα or Hβ emission line. Some broad-line sources have substantial dust obscuration, with attenuation reaching values around Av ≈ 4. Some objects display a distinctive V-shaped spectral energy distribution (e.g., D. D. Kocevski et al. 2023a; I. Labbe et al. 2024; P. G. Pérez-González et al. 2024), characterized by a sharp decline in rest-frame optical that may result from a dust-reddened active nucleus or intense dusty starburst activity. There is an additional rest-frame UV component, which could arise from residual star formation or AGN light that has been scattered and is less obscured (D. D. Kocevski et al. 2023a; J. E. Greene et al. 2024). Therefore, our observational comparison with these objects should be made with caution.

At all redshifts, TNG300-1 roughly matches observations, generally sitting slightly above the Global fit A line. X. Shen et al. (2020a) described the Global fit A as the best fit from their parametric model that uses a flexible polynomial at the faint end of the luminosity function.

The faint end of the luminosity function steepens with increasing redshift, consistent with M. Habouzit et al. (2022b).

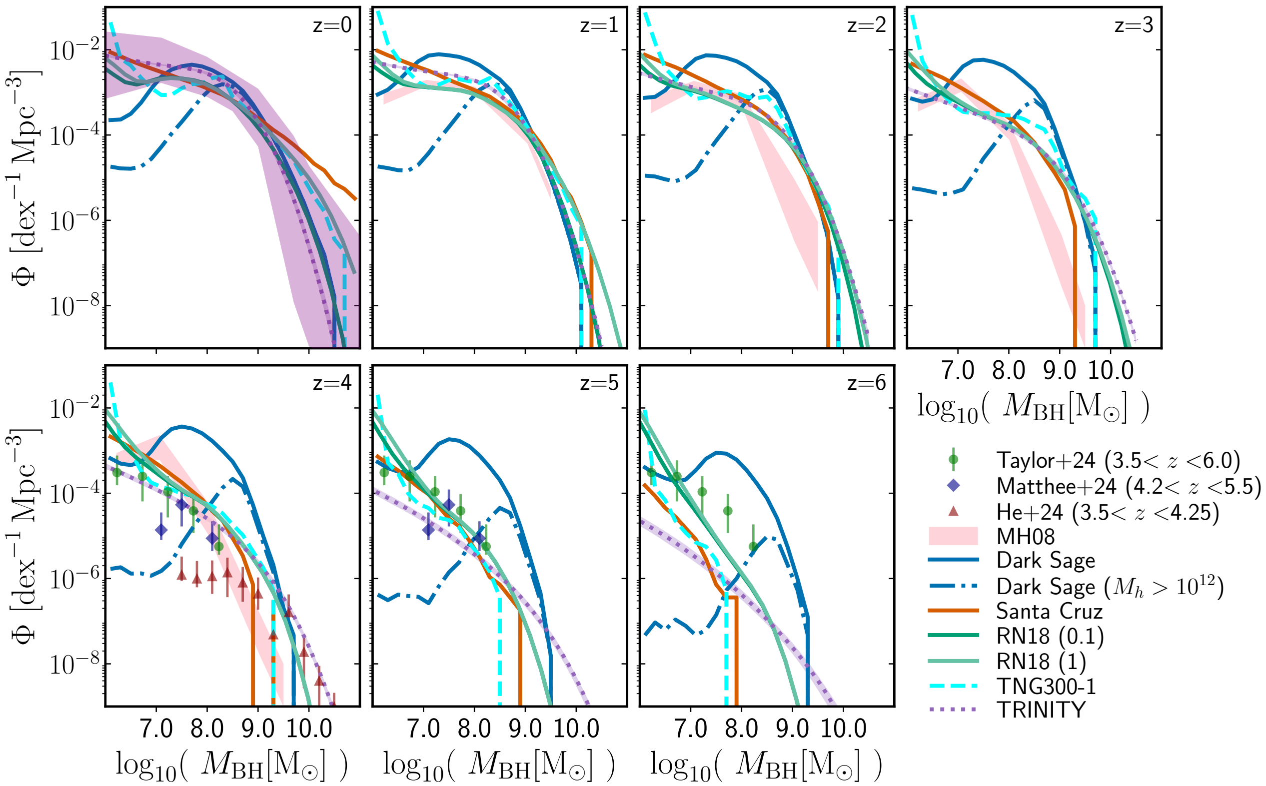

Figure 2. BHMFs from $z = 0$ to $z = 6$ for DARK SAGE (solid dark-blue line), DARK SAGE black holes in $M_h > 10^{12}\, M_\odot$ (dashed–dotted dark-blue line), the SANTA CRUZ SAM (solid brown line), and RN18 (solid green line: $p_{\rm merge} = 0.1$, solid light-green line: $p_{\rm merge} = 1.0$). We include TNG300-1 (dashed cyan line) and TRINITY (dotted purple line) in this comparison. The BHMF derived from the continuity equation in A. Merloni & S. Heinz (2008) for $1 < z < 4$ is shown in pink. We include the broad-line AGN BHMF for $3.5 < z < 6$ in green circles from A. J. Taylor et al. (2024). NIRCam WFSS from J. Matthee et al. (2024) for $4.2 < z < 5.5$ are shown as purple diamonds. Ground-based SDSS+HSC data from W. He et al. (2024) for $3.5 < z < 4.25$ are in red triangles. Note that the lowest-mass data point from A. J. Taylor et al. (2024) and J. Matthee et al. (2024) suffer from incompleteness. Models that show significant discrepancies at $z = 0$ align more closely at $z \sim 1$–4, except for the distinct bump in DARK SAGE.

The SANTA CRUZ SAM reproduces the observed AGN luminosity function at $z = 1$–6, in agreement with L. Y. A. Yung et al. (2021). At z = 4–5, the SANTA CRUZ SAM closely matches Y. Harikane et al. (2023) and J. Guo et al. (2024) observations, suggesting a higher number density of AGNs with low luminosity compared to X. Shen et al. (2020a). In DARK SAGE, a match to such high number densities is not possible likely due to the limitation from the resolution of the underlying dark matter merger tree simulation used. We find that the bright end of the quasar luminosity function becomes steeper at $z \gtrsim 2$, while the faint end steepens at $z \gtrsim 3$ and continues to do so at higher redshifts (X. Shen et al. 2020a). We notice that at $z = 2$–3, the faint-end slope in the SANTA CRUZ SAM is overpredicting the number density. Its slope stays consistently steep up to $z = 6$ when it finally matches the observations. At $z = 0$, the SANTA CRUZ SAM[8] matches the observed bright-end slope. Note that none of these models, with the exception of RN18, are tuned to match the observed bolometric quasar luminosity function, so it is surprising to see the level of agreement between some physics-based models and observations. RN18 is tuned to reproduce the $z = 0.1$ AGN bolometric luminosity function from P. F. Hopkins et al. (2007b) and Y. Ueda et al. (2014). However, at $z = 1$–6, it naturally matches the observed luminosity functions. It appears more discrepant at the high-luminosity end for redshifts $z = 1$–6, but RN18 determined that this was most likely due to a lack of massive halos in the simulation.

At some redshifts, DARK SAGE and RN18 underpredict the bright end of the observed luminosity function. In DARK SAGE, this may result from the exclusion of highly accreting black holes in low-mass halos, limited gas supply in galaxies hosting rapidly accreting black holes, or accretion variability on timescales shorter than the model time step. In RN18, this is due to limited effective volume.

Between $z = 0$–1, although DARK SAGE closely matches the observed bolometric AGN luminosity function at the high-luminosity end, at low-luminosities, it severely underpredicts the number density by ∼2 orders of magnitude. The low-luminosity end in DARK SAGE starts to converge with other models at $z \gtrsim 3$. By $z = 2$, the distinct "knee" near $M_{\rm BH} \sim 10^8\, M_\odot$ (Figure 2) becomes more pronounced, diverging from the observed single power-law distribution with increasing redshift. By $z = 5$–6, this feature is ∼2 orders of magnitude above the observations from X. Shen et al. (2020a); however, it is consistent with the inferred bolometric AGN luminosity function of the "little red dots" (H. B. Akins et al. 2024; J. E. Greene et al. 2024; V. Kokorev et al. 2024; J. Matthee et al. 2024). Note that here the "little red dots" are assumed to be actively accreting black holes with AGNs emitting the broad lines. The current literature remains uncertain of whether these "little red dots" are galaxies or AGNs (J. Silk et al. 2024).

---

[8] For Figures 3 and 3.4, we use only the "radiatively efficient" (merger and disk-instability triggered) accretion mode from the SANTA CRUZ SAM model, as we expect accretion associated with the "jet mode" to be radiatively inefficient.

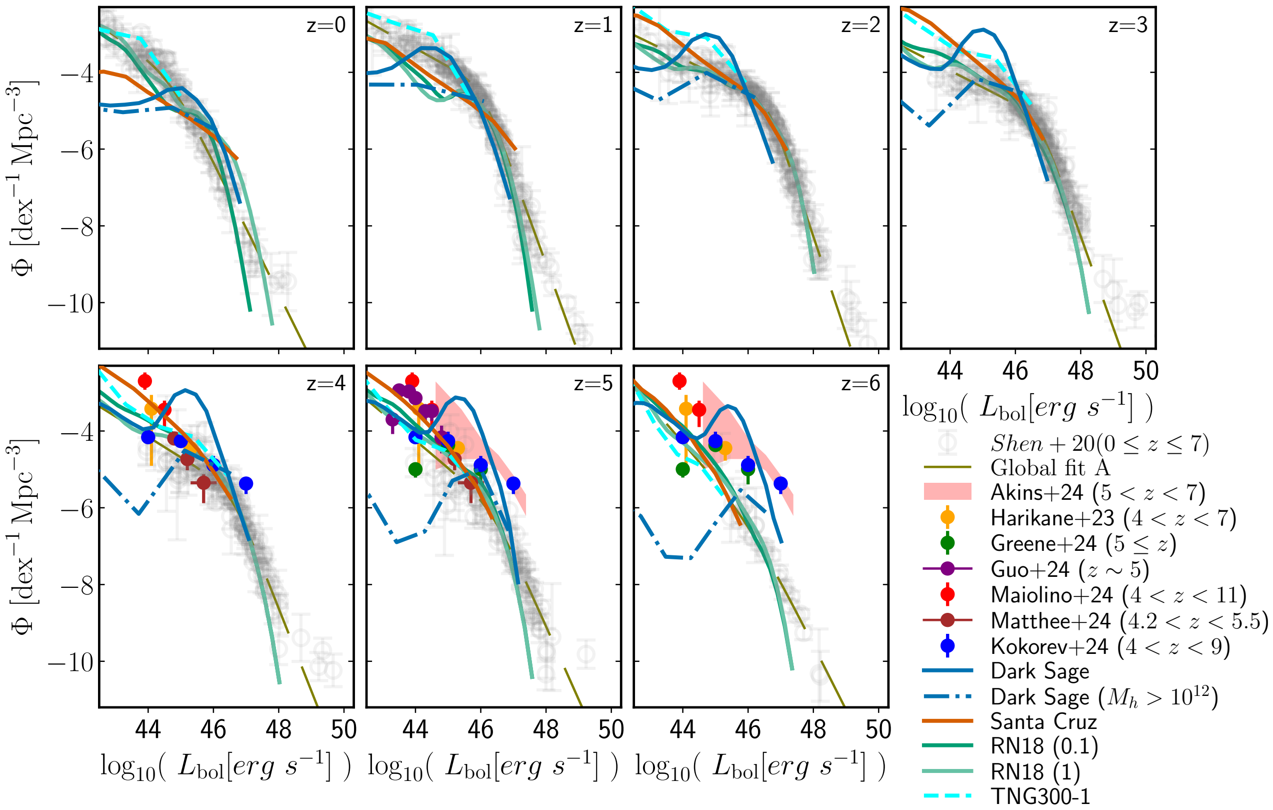

Figure 3. The bolometric AGN luminosity function at $z = 0$–6 for all models described in Figure 2. Here, we include observations from X. Shen et al. (2020a) in gray, which include the rest-frame IR, *B* band, UV, soft, and hard X-ray as well as bolometric, dust, and extinction corrections. We add the X. Shen et al. (2020a) Global fit A as a dashed olive line. The shaded red region at $z = 5$–6 is the inferred bolometric luminosity if we assume that the "little red dots" discovered by JWST are AGNs (H. B. Akins et al. 2024). We also include JWST observations from Y. Harikane et al. (2023), J. E. Greene et al. (2024), J. Guo et al. (2024), R. Maiolino et al. (2024), J. Matthee et al. (2024), and V. Kokorev et al. (2024) within their respective redshift. Overall, the TNG300-1 and the RN18 models agree with observations across time. The SANTA CRUZ SAM deviates from observations at $z = 0$ in the bright end of the bolometric AGN luminosity function but aligns with observations at higher redshifts. At $z \sim 5$–6, DARK SAGE's line surprisingly falls within the inferred bolometric AGN luminosity function from H. B. Akins et al. (2024) and V. Kokorev et al. (2024).

We now explore the assembly of SMBHs as a function of the final host dark-matter halo mass over redshift, from which we gain insights into SMBH–galaxy coevolution. We plot the median black hole mass of the largest progenitor galaxy for a root $M_h \sim 10^{12-15}\,M_\odot$ halo at $z = 0$ in Figure 4. Note that, at $z = 0$, our Galaxy's dark matter halo is $M_h \sim 10^{12}\,M_\odot$ (B. Little & S. Tremaine 1987; A. S. Kulessa & D. Lynden-Bell 1992; A. Klypin et al. 2002; M. Boylan-Kolchin et al. 2013; J. Shen et al. 2022a) and M87's dark matter halo mass from the Virgo cluster is $M_h \sim 10^{15}\,M_\odot$ (W. G. Mathews 1978; P. Fouqué et al. 2001; E. J. Shaya et al. 2017; O. G. Kashibadze et al. 2020). The manner in which black hole masses assemble in these halos is determined by the timing difference in how the halos themselves assemble. Although models generally converge within an order of magnitude in their predicted final SMBH masses across all halo mass bins except the highest, their respective growth histories differ significantly.

First, we note that in DARK SAGE, black hole growth over the range $1 \leqslant z \leqslant 6$ is steadily increasing independent of halo mass, unlike the SANTA CRUZ SAM and RN18, which show a steeper median distribution with increasing halo mass. In contrast, black holes in TNG300-1 stall at $M_{\rm BH} \sim 10^6\,M_\odot$ until $z < 2$. After this point, they gain between 1–4 orders of magnitude in mass, depending on their host halo mass. At $z > 1$, the normalization of the median black hole mass in DARK SAGE increases with halo mass. This arises because halos that are more massive at $z = 0$ experience higher merger rates and earlier gas assembly, leading to enhanced cold-mode and instability accretion at high redshift (Figure 8). In DARK SAGE, all black hole growth channels depend either explicitly or implicitly on dark matter halo properties such as the virial temperature or virial velocity, with the resulting dependence on halo mass mediated through merger-driven triggering and the availability of cold gas for accretion. While the DARK SAGE median black hole mass is consistent with the mass of M87* for halos with $M_h \sim 10^{15}\,M_\odot$, the model overpredicts the mass of Sgr A* by about 1.5 dex at $z = 0$. Note that median distributions may be sensitive to the halo mass resolution, so interpretations of median trends in DARK SAGE at $z > 1$ should be made with caution.

In most cases, DARK SAGE, the SANTA CRUZ SAM, and RN18 show a sharp increase in the median black hole mass growth at $z < 1$. In contrast, TRINITY shows a flattening curve in this redshift range, indicating a slowdown in growth. SMBHs grow rapidly, with the growth rate depending on the mass of the halo mass they reside in. For example, in more-massive halos, the SMBH growth phase ends above $z > 3$.

In Milky Way–like halos, most models produce SMBHs that are slightly more massive than Sgr A*. This is likely because Sgr A* is undermassive compared to black holes in the global $M_{\rm BH}$–M_* or $M_{\rm BH}$–$M_{\rm bulge}$ relation. DARK SAGE has the highest median curve due to its super-Eddington accretion at high-z and its orders-of-magnitude drop to sub-Eddington at lower-z (see Figure 5). In the case of TNG300-1, its initial black hole

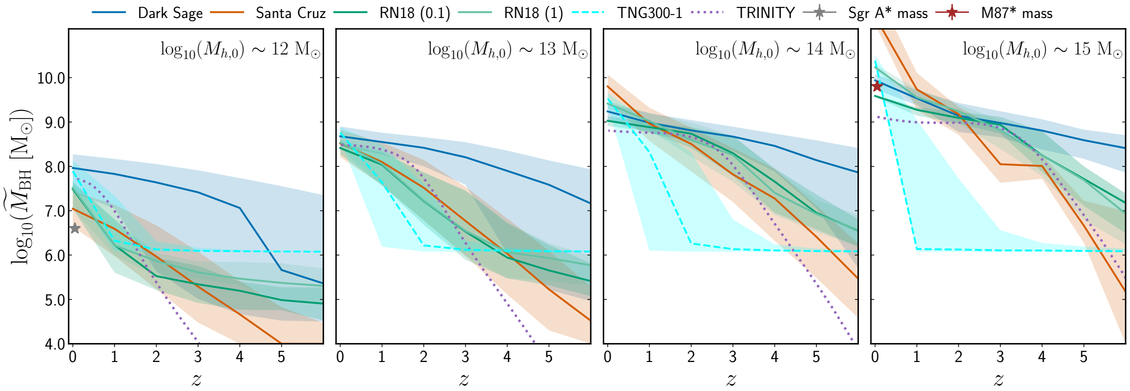

Figure 4. Median black hole mass growth history as a function of redshift. Each panel shows a fixed halo mass from $M_h \sim 10^{12-15}\,M_\odot$ taken at $z = 0$ for semianalytic models DARK SAGE (solid dark-blue line), the SANTA CRUZ SAM (solid brown line), and RN18 (solid green line: $p_{\rm merge} = 0.1$, solid light-green line: $p_{\rm merge} = 1.0$). The shaded regions enclose 68% of the data. We compare those models to TNG300-1 (dashed cyan line) and TRINITY (dotted purple line). The gray star represents Sgr A*, which is hosted in a halo with $M_h \sim 10^{12}\,M_\odot$, while the dark-red star represents M87*, hosted in a halo with $M_h \sim 10^{15}\,M_\odot$. For a more complete representation of this figure, note the black hole seeding mass denoted in Table 1. In most cases, all models converge within an order of magnitude in the final black hole mass at $z = 0$. However, in the highest halo mass bin, the difference extends to 2 orders of magnitude.

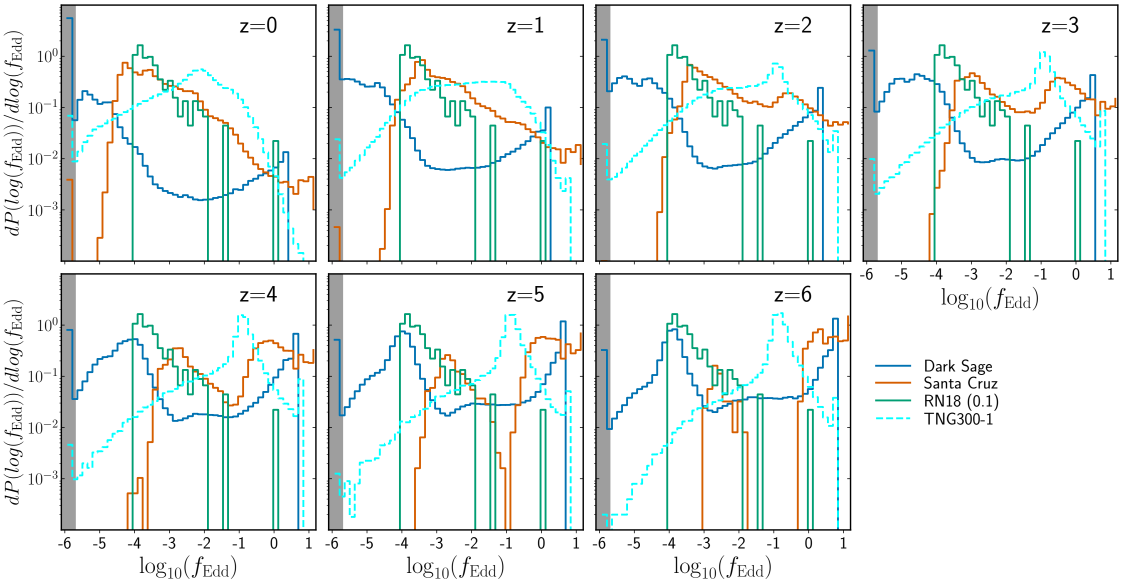

Figure 5. Histograms of the Eddington ratio distributions from $z = 0$ to $z = 6$ for DARK SAGE (solid dark-blue line), the SANTA CRUZ SAM (solid brown line), and RN18 (solid green line: $p_{\rm merge} = 0.1$. Note that the RN18 model with $p_{\rm merge} = 1.0$ has Eddington ratio distributions similar to the model with $p_{\rm merge} = 0.1$. Therefore, we have chosen to present only one of these models. The gray region represents black holes with $\log_{10}(f_{\rm Edd}) \leqslant -6$. Here, we impose a lower-mass threshold of $\log_{10}(M_{\rm BH}) > 6.0$. We compare those models to TNG300-1 (dashed cyan line). Not surprisingly, we see high variation in the Eddington ratio distributions between models at all redshifts.

seeding mass is already close to the Sgr A* mass (see Table 1); thus, we see less growth across time. In RN18, we see a flattened median line that slightly increases with redshift until it converges at $z = 1$. In the SANTA CRUZ SAM, black holes gain 3 orders of magnitude of steady growth from $z = 5$ up to $z = 0$.

For halos with $M_h \sim 10^{14}\,M_\odot$, the median black hole mass in the DARK SAGE model increases by ≈4.5 dex from $z = 6$ to $z = 0$ similar to results from the SANTA CRUZ SAM. Both RN18 models gain about ≈2.5 dex within this halo mass and redshift range. Below $z = 2$, DARK SAGE, RN18, and the SANTA CRUZ SAM start to diverge for $M_h \sim 10^{14-15}\,M_\odot$, indicating a higher rate of BH–BH mergers in this regime. This shows more clearly for $M_h \sim 10^{15}\,M_\odot$, where the RN18$p_{\rm merge} = 1$ model clearly produces higher-mass black holes compared to $p_{\rm merge} = 0.1$. In galaxy clusters, black hole mass growth flattens at low redshift for RN18 but steepens in DARK SAGE, the SANTA CRUZ SAM, and TNG300-1. In RN18, this flattening follows strict adherence to the M–σ, while other models steepen due to frequent black hole mergers and the absence of dynamics delaying mergers after galaxy mergers. The contribution of BH–BH mergers to the total black hole mass growth in DARK SAGE is clearly shown in Figure 8. Within the highest halo mass bin, the SANTA CRUZ SAM predicts a median black hole mass that is ∼1.6 dex higher than M87* mass, while TRINITY predicts a black hole mass an order of magnitude lower. At all halo masses, DARK SAGE predicts the largest amount of scatter in black hole mass at fixed halo mass, around ∼3 dex above $z = 1$.

3.3. Eddington Ratio Distributions

Figure 5 highlights a diverse set of $\log_{10}(f_{\rm Edd})$ distributions between models. We show the Eddington ratio distributions for all galaxies as a function of cosmic epoch. At $z = 0$, DARK SAGE shows a slight bimodal peak between $\log_{10}(f_{\rm Edd}) \sim -5.5$

and −4.5. The SANTA CRUZ SAM shows a skewed distribution peaking around $\log_{10}(f_{\rm Edd}) \sim -4, -3$. RN18 overlaps with the SANTA CRUZ SAM peaking at $\log_{10}(f_{\rm Edd}) \sim -3.5$. TNG300-1 shows a broad distribution that peaks around $\log_{10}(f_{\rm Edd}) \sim -2$. As redshift increases, the TNG300-1 distribution narrows and shifts to be an order of magnitude higher in $\log_{10}(f_{\rm Edd})$ by $z = 6$. The SANTA CRUZ SAM distributions become bimodal around $z = 2$, and by $z = 6$, at or above the Eddington limit. By construction, the RN18 distributions maintain a peak at $\log_{10}(f_{\rm Edd}) \sim -4$ across all redshifts, with a narrow peak around $\log_{10}(f_{\rm Edd}) \sim 0$. Lastly, with increasing redshift, more black holes in DARK SAGE accrete above the Eddington limit.

For the SANTA CRUZ and DARK SAGE SAMs, the bimodal and trimodal distributions of the black hole growth appear to depend on halo mass. In the case of DARK SAGE (see Appendix B), at $z < 3$, when breaking down the Eddington ratio distributions into halo mass bins, the distribution more tilted toward sub-Eddington values (the leftmost one) corresponds to black holes in high-mass halos around $M_h \sim 10^{14}\,M_\odot$, whereas the other sub-Eddington distribution at $\log(f_{\rm Edd}) \approx -4$ arises from black holes in low-mass halos around $M_h \sim 10^{12}\,M_\odot$. Similarly, in the SANTA CRUZ model, high-mass halos $M_h > 10^{13}\,M_\odot$ display higher Eddington ratio distributions compared to halos around $M_h \sim 10^{12}\,M_\odot$. The observed bimodality in RN18, the SANTA CRUZ SAM, and DARK SAGE is due to a rapid accretion mode triggered by galaxy–galaxy mergers.

3.4. The Integrated Cosmic SMBH Mass Density

The integrated mass density of SMBHs at a particular redshift is computed by summing over mass growth via accretion processes that have occurred over preceding cosmic times. More specifically, for a given bolometric AGN luminosity function $\Phi(L, z)$, the cumulative mass density can be derived by integrating over a range of bolometric luminosities and redshifts, taking into account parameters such as the radiative efficiency, kinetic efficiency, and time elapsed in the Universe.

Figure 6 shows the cosmic SMBH mass and accretion density as a function of time for various physics-based and empirical models. The left panel includes F. Shankar et al. (2013), A. Merloni & S. Heinz (2008), and A. Marconi et al. (2004), which solves the continuity equation. The empirical cosmic SMBH mass density is obtained using the intrinsic X-ray luminosity function in the rest-frame 2–10 keV band with a bolometric correction following Equation (8):

$$\rho_{\rm BH}(z) = \int_z^{z_S}\int_{L_{\rm min}}^{L_{\rm max}} \frac{(1-\eta-\eta_{\rm kin})}{\eta}\frac{L}{c^2}\Phi(L, z)\,d\log L \times \frac{dt}{dz}dz. \quad (8)$$

where L is the bolometric luminosity, z_S is the redshift upper limit at which significant black hole growth begins, η is the radiative efficiency as mentioned in the above paragraphs, and c is the speed of light. T. T. Ananna et al. (2020) integrated over bolometric luminosities 10^{42}–10^{50} erg s^{-1} in Equation (8) to obtain the cosmic SMBH mass density results shown in the left panel of Figure 6. One can also change Equation (8) to obtain the cosmic SMBH mass density with a dependence on the black hole accretion history, in the form of $\rho_{\rm BH}(z)$ using two parameters: the local black hole mass density $\rho_{\rm BH,0}$ and the (average) radiative efficiency $\epsilon_{\rm rad}$. This leads to an intriguing implication: without assuming anything about the distribution of the Eddington ratios in the AGN population, constraints can be obtained on the (mass-weighted) average radiative efficiency. The Soltan argument (A. Merloni & S. Heinz 2008) establishes a robust lower limit for $\epsilon_{\rm rad}$. Specifically, it is enough to identify the value of the radiative efficiency that renders the integral $\int_0^z \frac{\Psi_{\rm BHAR}(z')}{\rho_{\rm BH,0}}\frac{dt}{dz'}dz'$ greater than unity. A. Merloni & S. Heinz (2008) obtained a lower limit of 0.065 with the chosen local SMBH mass function and AGN bolometric luminosity function.[9]

Current estimates for the empirical local black hole mass density ($\rho_{\rm BH}$) converge at $z = 0$ to within about 1 dex with estimates between 5–6 × $10^{10}\,M_\odot$ Mpc^{-3} (A. Merloni & S. Heinz 2008; F. Shankar et al. 2013; H. Zhang et al. 2023; A. Marconi et al. 2004). The cosmic SMBH density function obtained from T. T. Ananna et al. (2020) is derived using a range of radiative efficiencies between 0.1 and 0.3. TRINITY includes the contribution of wandering black holes in their results, which accounts for about 15% of the total black hole mass density at $z = 0$ (H. Zhang et al. 2023). Their results are stated to be consistent with M. Volonteri et al. (2003) and A. Ricarte et al. (2021). Below $z \sim 2$, discrepancies in mass density comparisons across various studies are likely to arise from differences in models with varying efficiencies in AGN energy, occupation fraction of unobscured AGNs, and/or the missing contribution of black holes in low-mass halos. Above $z \sim 2$, the consistent difference between A. Marconi et al. (2004) and other models becomes more noticeable. This discrepancy is possibly a result of their approach to modeling AGN evolution, assuming that SMBH growth took place before $z \sim 3$. However, these initial assumptions did not consider the mass growth history of SMBHs at higher redshifts, which explains the difference in SMBH mass distribution between A. Marconi et al. (2004) and other models like TRINITY, where SMBHs start growing as early as redshift 15. The high-redshift plateau seen in the RN18 models occurs because the mass density at these early epochs is dominated by seeds. Mass locked up in seeds is invisible to mass density estimates inferred from radiation and is thus unaccounted for in empirical models. Physics-based models either have light seeds or do not resolve the halos at epochs and masses where the seeds dominating the RN18 mass density reside. Our results are consistent with P. Natarajan et al. (2023), where even models that roughly reproduce the observed local SMBH mass density at $z \sim 0$ begin to diverge significantly by $z \sim 3$, differing by several orders of magnitude.

At $z = 0$, DARK SAGE, the SANTA CRUZ SAM and TNG300-1 closely agree to about $\log_{10}(\rho_{\rm BH}) \approx 6$. DARK SAGE[10] lies 0.2 dex lower than the SANTA CRUZ SAM and TNG300-1. F. Shankar et al. (2013) and H. Zhang et al. (2023) agree with $\log_{10}(\rho_{\rm BH}) \approx 5.7$, whereas RN18 models predict 0.5 dex lower black hole mass density than the SANTA CRUZ SAM and

---

[9] In our simulations, we calculate the cosmic SMBH mass density by binning black holes by redshift, summing their mass and dividing by the volume of the corresponding simulation box. Empirical curves in Figure 6 are retrieved from the literature.

[10] In DARK SAGE, there is a 0.05 dex difference in the $z = 0$ cosmic SMBH density if we remove our halo mass cut.

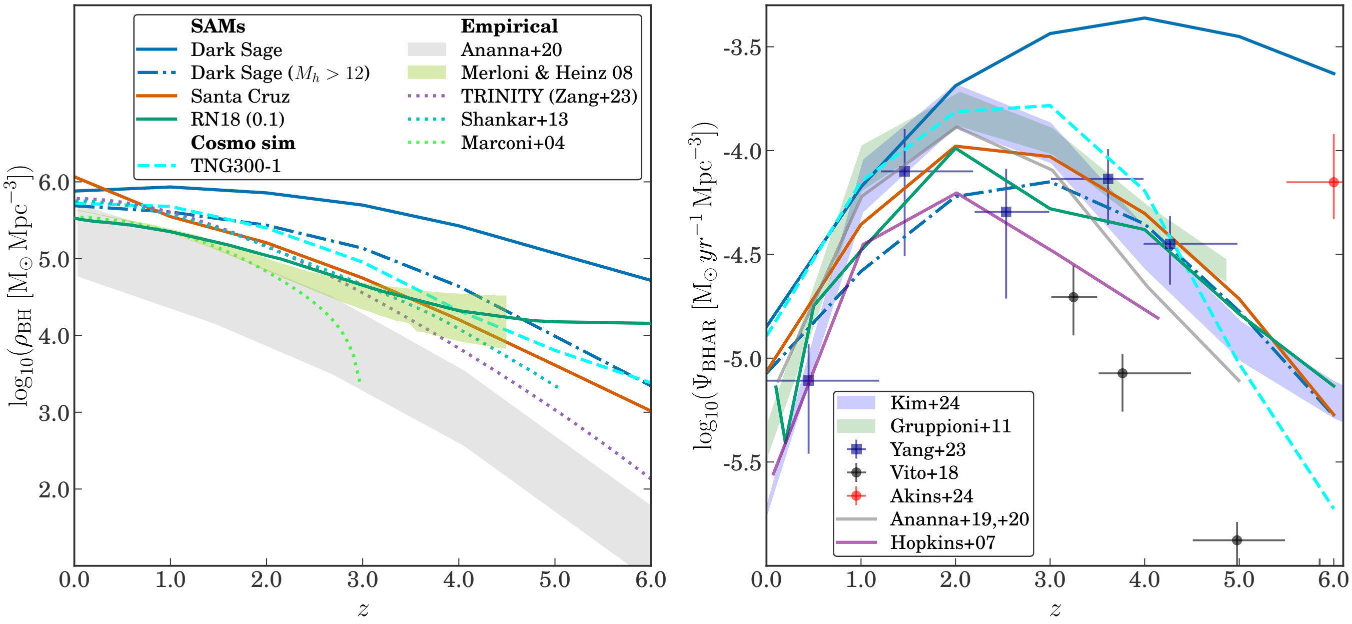

Figure 6. The cosmic SMBH mass and accretion density function for physics-based models and observations. The left panel includes H. Zhang et al. (2023; TRINITY, dotted purple line), T. T. Ananna et al. (2020; shaded yellow-green region), F. Shankar et al. (2013; dotted cyan line), A. Merloni & S. Heinz (2008; shaded aquamarine region), and A. Marconi et al. (2004; dotted lime line) empirical models compared to semianalytic models DARK SAGE (solid dark-blue line), DARK SAGE black holes in $M_h > 10^{12}\ M_\odot$ (dashed–dotted dark-blue line), the SANTA CRUZ SAM (solid brown line), and RN18 (solid green line: $p_{\rm merge} = 0.1$. The dashed cyan line shows TNG300-1. The right panel shows same physics-based models, while including observations from P. F. Hopkins et al. (2007b), C. Gruppioni et al. (2011), F. Vito et al. (2018), T. T. Ananna et al. (2019, 2020), G. Yang et al. (2023), S. J. Kim et al. (2024), and H. B. Akins et al. (2024). For the cosmic SMBH mass density, models with different $\log_{10}(\rho_{\rm BH})$ histories converge at $z = 0$. Most models agree with observations for the black hole accretion rate density, except for SANTA CRUZ at $z = 0$ and DARK SAGE at $z > 2$. In both panels, DARK SAGE recovers the observed normalization by only including black holes in $M_h > 10^{12}\ M_\odot$.

TNG300-1, in agreement with A. Marconi et al. (2004), A. Merloni & S. Heinz (2008), and T. T. Ananna et al. (2020). By $z > 3$, T. T. Ananna et al. (2020) has the lowest number density of all. In this redshift range, the cosmic mass density normalization from F. Shankar et al. (2013), T. T. Ananna et al. (2020), and TRINITY is slightly off by about 0.1 dex

The right panel presents the cosmic SMBH accretion histories. S. J. Kim et al. (2024) used a model to interpret mid-infrared galaxy source counts across a wide flux range, using extremely faint galaxies (C.-T. Ling et al. 2022, 2023; C. K. W. Wu et al. 2023). By applying a backward evolution model of parameterized mid-infrared luminosity functions, following C. Gruppioni et al. (2011), they fit this model to JWST/MIRI source counts alongside data from the Infrared Space Observatory, AKARI, and Spitzer (S. J. Oliver et al. 1997; S. Serjeant et al. 2000; B. Rocca-Volmerange et al. 2007; C. P. Pearson et al. 2010, 2014; H. Davidge et al. 2017), providing constraints to the cosmic star formation history and black hole accretion history. C. Gruppioni et al. (2011) modeled the local galaxy luminosity function for mid-infrared bands for five different types of galaxies. Then, they approximated the bolometric luminosity to the infrared luminosity integrated between 1 and 1000 μm. Because their samples have different galaxies, the AGN contribution to the luminosity is weighted. G. Yang et al. (2023) points are derived from MIRI-selected AGNs. The points of F. Vito et al. (2018) and P. F. Hopkins et al. (2007b) come from X-ray detections.

From $z = 0$ to $z = 1$, observations agree within ≈0.4 dex from each other. By $z > 1$, observations start to diverge, where S. J. Kim et al. (2024), T. T. Ananna et al. (2020), and C. Gruppioni et al. (2011) showed values that are higher than those of F. Vito et al. (2018) and P. F. Hopkins et al. (2007b). Such differences may arise from variations in methodology, wavelength coverage, and the datasets used. RN18 is the only model that spans the range of the observed black hole accretion density from $z = 0$–6. While TNG300-1 is slightly higher than most observations at $z = 0$, it matches S. J. Kim et al. (2024) and C. Gruppioni et al. (2011) between $z \approx 3$–5. The SANTA CRUZ SAM matches observations from G. Yang et al. (2023) black hole accretion density at $z > 1$. By $z = 0$, the model lies about 0.2 dex below DARK SAGE and TNG300-1, whose models overpredict the number density of accreting black holes compared to observations. Between $z = 1$–2, DARK SAGE agrees with S. J. Kim et al. (2024) and C. Gruppioni et al. (2011). However, above $z = 2$, a large number of black holes continue to accrete highly up until $z = 3$. The black hole accretion density for "little red dots" lies orders of magnitude above all observations (H. B. Akins et al. 2024), closer to DARK SAGE prediction. While most physics-based models derived accretion density peak at $z \sim 2$ like in the observations, DARK SAGE shows an earlier peak around $z \sim 4$ due to its high number of low-mass halos and black holes growing rapidly at earlier times.

The differences in results between observations and DARK SAGE are primarily due to sample selection. As illustrated in the dashed–dotted dark-blue line, where we take only black holes with $M_h > 10^{12}\ M_\odot$, we find a closer match to the observations in the cosmic SMBH mass and accretion density, consistent with previous results from J. Wolf et al. (2023), who took a sample of massive halos from the Horizon-AGN (M. Volonteri et al. 2016) and Astrid (Y. Ni et al. 2022) to match the observed black hole accretion rate density. General discrepancies between physics-based models likely arise from how each of the models account for coevolutionary processes

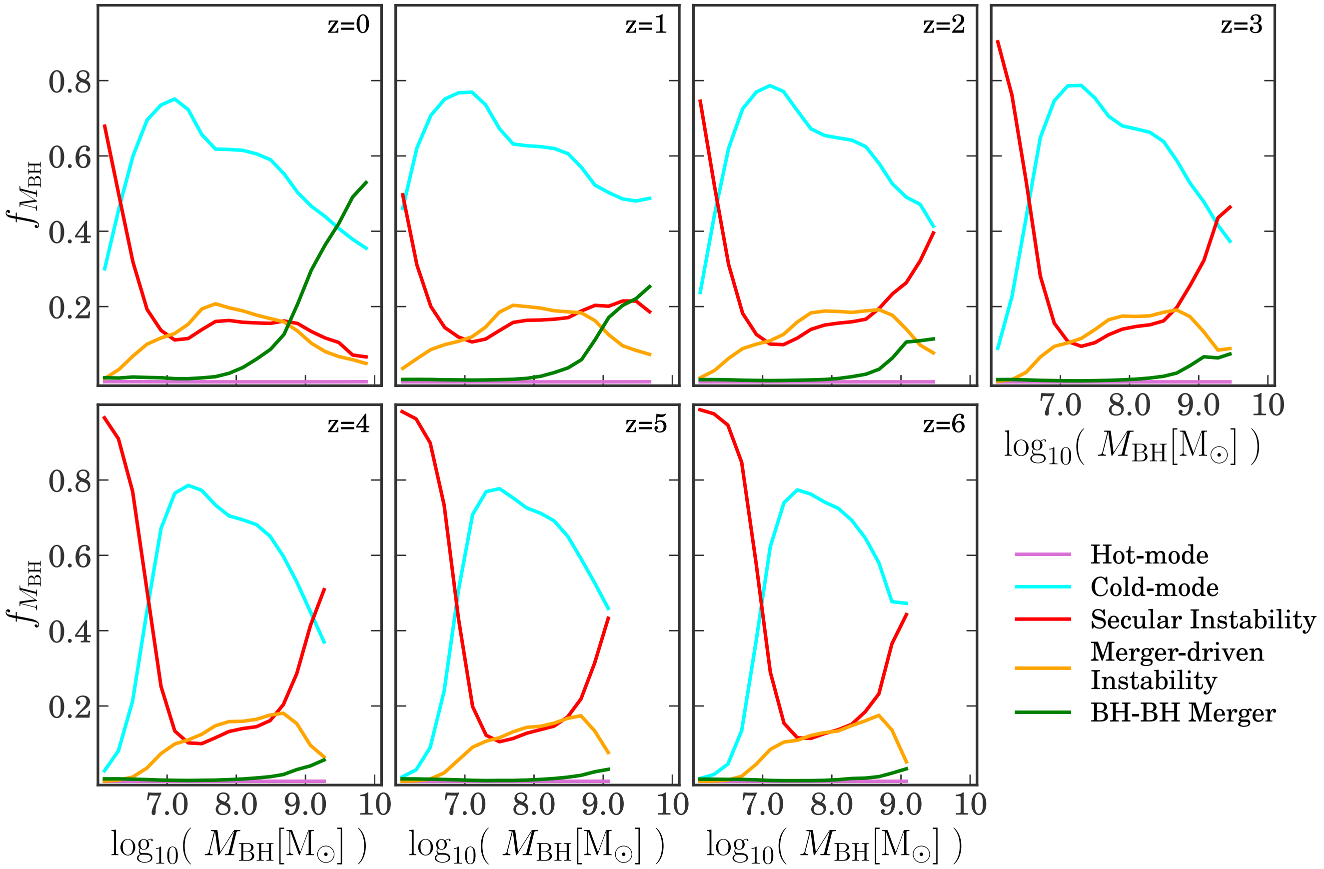

Figure 7. The fraction of black hole mass contributed by the five, different, distinct black hole growth channels in DARK SAGE: hot mode (solid violet line), cold mode (solid cyan line), secular instability mode (solid red line), merger-driven instability mode (solid yellow line), and BH–BH merger mode (solid green line). These are binned by black hole mass for $z = 0$ to $z = 6$. At all redshifts for the fiducial model, black holes that are $\sim 10^6\, M_\odot$ grow through secular instabilities. At the high-mass end, the cold mode, BH–BH mergers, and secular instabilities contribute the most to the final black hole mass budget across redshift.

between black holes and their host galaxies, such as the black hole mass–stellar/bulge mass relation at $z = 0$ and/or variation in the black hole merger rate and its contribution to black hole growth. Variances in the strength or timing of feedback processes in physics-based models also appear to contribute to differences in the predictions.

4. Focusing on the SMBH Assembly in DARK SAGE

With DARK SAGE, we investigate how different growth channels contribute to final SMBH masses across redshift. In Figure 7, we present the fraction of black hole mass divided by the contributions from five distinct growth channels in DARK SAGE: hot mode, cold mode, secular instability mode, merger-driven instability mode, and BH–BH merger mode. Regardless of redshift, black holes with masses around $\sim 10^6\, M_\odot$ primarily grow through secular instabilities. For $M_{\rm BH} > 10^6\, M_\odot$, DARK SAGE reveals a diversity of growth paths. At $z = 0$, most of the growth in $M_{\rm BH} > 10^{9.5}\, M_\odot$ is driven by BH–BH mergers and cold-mode accretion. The contribution from BH–BH mergers decreases with lower black hole mass and increasing redshift, becoming nearly insignificant by $z = 3$. The large contribution of BH–BH mergers to the final black hole mass census at low redshift agrees with predictions from other physical models, both numerical hydrodynamics and semianalytic models (A. Ricarte & P. Natarajan 2018; R. Weinberger et al. 2018; F. Pacucci & A. Loeb 2020).

In all cases, the hot-mode growth channel contributes the least to the final mass. Across redshifts, the cold-mode channel consistently adds to the black hole mass budget, contributing up to 80% of the final mass for $M_{\rm BH} \sim 10^{7-8}\, M_\odot$. This gas is residual from recently merger galaxies. Recall that cold mode and accretion due to merger-driven instabilities occurs only when there is a galaxy merger and/or there is unstable cold gas mass with a low Q Toomre parameter and low angular momentum that is feeding the black hole episodically. Even in the absence of galaxy mergers, DARK SAGE SMBHs may still grow through secular accretion of unstable cold gas.

Figure 8 displays the median black hole mass as a function of halo mass and redshift for each of the black hole growth channels. For most SMBHs, we find that the cold-mode, merger-driven, and secular instabilities contribute most significantly to mass growth. Bondi accretion from the halo, hot mode, provides the least mass across redshift. Recall that the cold-mode and merger-driven instabilities occur only when there is a galaxy merger. After a galaxy merger, a fraction of the total cold gas mass from the secondary galaxy, $f_{\rm BH}$, is added directly into the primary black hole. The remaining cold gas is added into the primary's cold gas annuli. DARK SAGE enters a starburst phase. Then, it calculates the Q Toomre parameter. Any unstable cold gas that is not resolved by mass transfer from neighboring annuli or by a starburst is transferred to the lowest angular momentum annuli. Thereafter, such unstable gas is added into the primary black hole. Even in the absence of galaxy mergers, black holes may still grow through

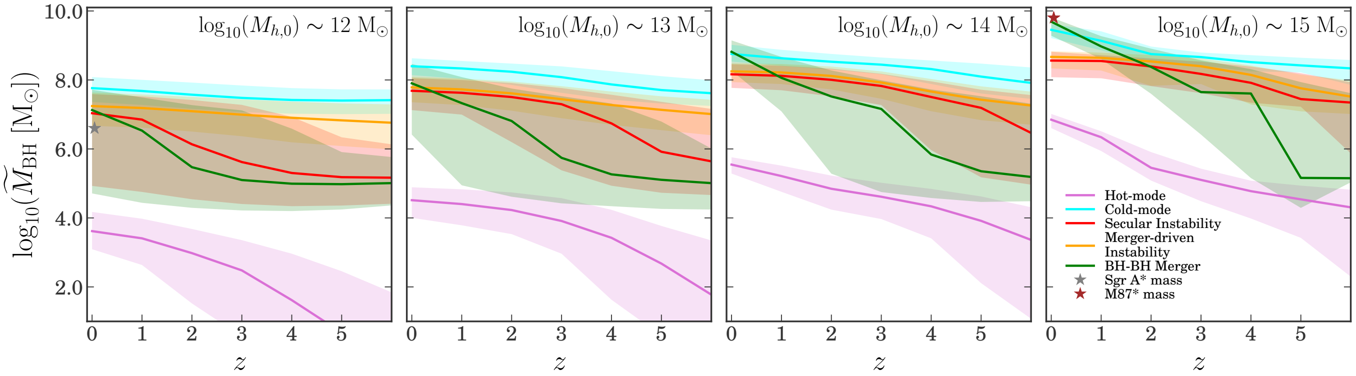

Figure 8. Median black hole mass growth history separated by the five black hole growth channels described in Figure 7. The shaded regions enclose 68% of the data. The gray star represents the black hole mass of Sgr A*, and the dark-red star represents the black hole mass of M87*, each at their respective halo masses. Generally, both cold mode and instabilities contribute the most mass to black hole mass across redshift.

secular instabilities of unstable cold gas. Figure 8 shows that merger-driven and secular instabilities contribute almost equally for $M_h \approx 10^{15}\,M_\odot$. Their contribution is more significant for the low-mass halos.

For $z \sim 0$ and $M_h \approx 10^{14}\,M_\odot$, black hole mergers overtake all other growth channels. This agrees with other physical models, both hydrodynamic and semianalytic (A. Ricarte & P. Natarajan 2018; R. Weinberger et al. 2018; F. Pacucci & A. Loeb 2020).

Keeping in mind the pronounced super-Eddington peak at high redshift illustrated in Figure 5, we now turn to dissecting its source. Figure 9 shows the instantaneous Eddington ratio distributions for the black hole growth channels in DARK SAGE. At all redshifts, sub-Eddington accretion comes from the hot-mode channel, while super-Eddington accretion results primarily from cold-mode accretion and secular instabilities. Similar to Figure 5, a super-Eddington peak appears starting at $z = 1$. Above $z = 1$, cold-mode accretion dominates over instabilities. Throughout, merger-driven instability accretion remains to be a similar contributor to secular instabilities in the overall accretion budget.

Allowing for super-Eddington accretion carries significant implications for observing SMBHs. Super-Eddington accretion could explain the high number density of AGNs observed, especially within the "little red dots" population, where it could signify a short-lived stage in the early development of black holes. Although some objects have been observed in the X-ray (D. D. Kocevski et al. 2023b; T. T. Ananna et al. 2024; Á. Bogdán et al. 2024; O. E. Kovács et al. 2024), most of the AGNs identified by JWST have not been observed in the X-ray or detected in the radio (G. Mazzolari et al. 2024).

In theory, black holes accreting at super-Eddington develop accretion flows that are geometrically and optically thick as well as radiatively inefficient because of photon trapping (1979; M. A. Abramowicz et al. 1988). Recent work suggests that this distinctive accretion structure may give rise to softer X-ray emission (F. Pacucci & R. Narayan 2024), marked by steeper photon slopes and lower-energy spectral cutoffs, resulting in excessive cooling of the hot plasma near the black hole (P. Madau & F. Haardt 2024). Similar spectral features have been reported in AGN surveys focused on luminous quasars at $z \gtrsim 7$ (L. Zappacosta et al. 2020, 2023) as well as nearby SMBHs thought to be accreting above the Eddington limit (A. Tortosa et al. 2023). However, a complete picture of the broadband observational signatures of super-Eddington accretion remains unclear. Although some super-Eddington accretion candidates have been identified around $z \sim$ 4–6, their UV, optical, and X-ray fluxes vary significantly (J.-J. Tang et al. 2019; H. Suh et al. 2025).

5. Discussion and Conclusions

We study the mass evolution of SMBHs using a variety of semianalytic models, e.g., DARK SAGE, the SANTA CRUZ SAM, and RN18. We focus on the local and evolving BHMF, bolometric AGN luminosity, median black hole mass growth histories, Eddington ratio distributions, cosmic SMBH mass, and accretion rate histories. We compare model predictions with a set of inferred BHMFs from scaling relations and luminosity from the AGN. We include the most up-to-date inferred JWST results for the BHMF, the bolometric AGN luminosity function, and the cosmic black hole accretion rate history. Then, using DARK SAGE, we dissect the contribution of the black hole mass from the various growth channels implemented in the model. We present black hole mass fractions from each growth channel, median black hole mass growth histories, and Eddington ratio distributions across time.

Our key results can be summarized as follows:

1. The variations in the observationally inferred local BHMF are due to (a) fitting to SMFs with varying numbers of massive galaxies and (b) tuning to scaling relations with varying steepness in their fitting slopes. Physics-based models lie within the range of observational values. Their differences are also affected by the choice of SMFs and scaling relations when calibrating (Figure 1).
2. Despite the large variations in the local BHMF, in general, physics-based models tend to converge between z = 1–4, with the exception of DARK SAGE. By z = 4–5, A. Merloni & S. Heinz (2008), TRINITY, RN18, the SANTA CRUZ SAM, and TNG300-1 roughly agree with the BHMF derived from broad-line AGNs detected by JWST (W. He et al. 2024; J. Matthee et al. 2024; A. J. Taylor et al. 2024; Figure 2).
3. Above $z = 2$, DARK SAGE has a distinct "knee" near $M_{\rm BH} \sim 10^8\,M_\odot$ that remains fixed over time, becoming progressively narrower with increasing redshift and resulting in a sharper high-mass dropoff. This bump is also apparent in the bolometric AGN luminosity around $L_{\rm bol} \sim 10^{46}\ {\rm erg\ s^{-1}}$. Between z = 5–6, the bump in DARK SAGE matches the inferred AGN emission from "little red dots" (H. B. Akins et al. 2024). Roughly all physics-based models, with the exception of the SANTA CRUZ SAM at $z = 0$ and DARK SAGE above $z = 2$, match the

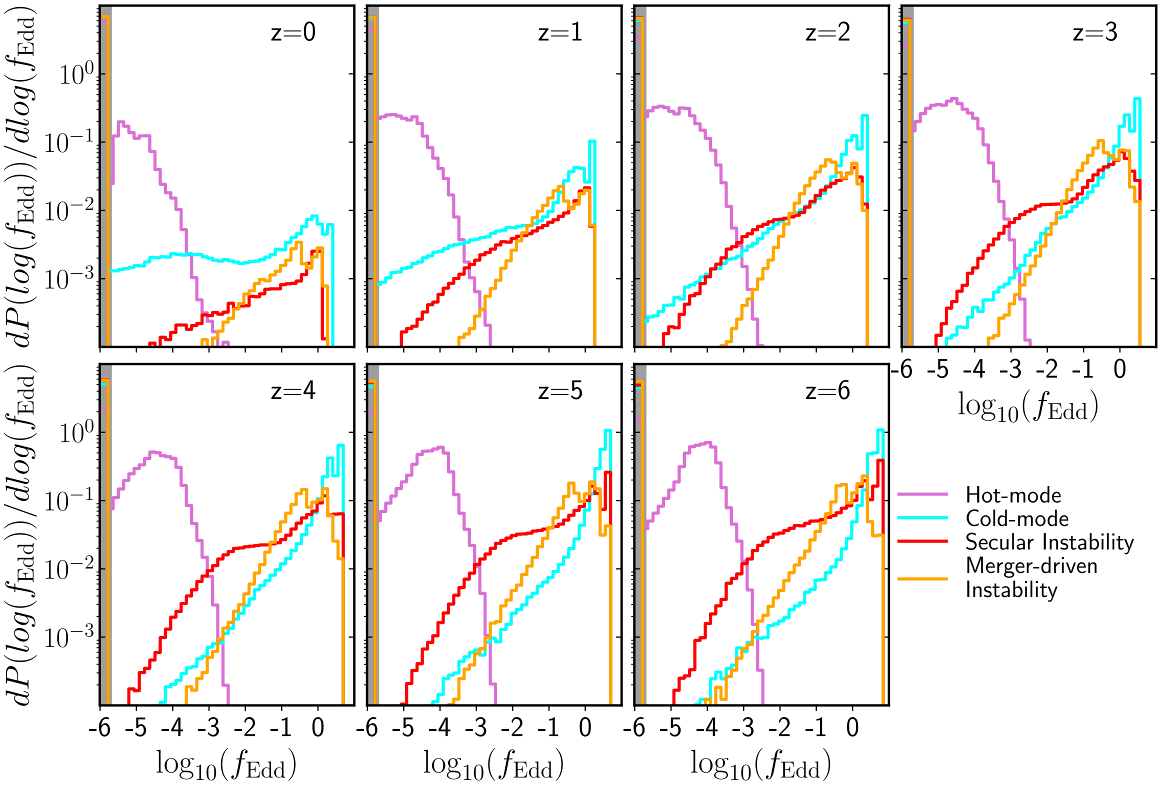

Figure 9. Histograms of the Eddington ratio distributions from $z = 0$ to $z = 6$ separated by the same distinct black hole growth channels presented in Figure 7, except BH–BH mergers. Here, we impose a lower-mass threshold of $\log_{10}(M_{\rm BH}) > 6.0$. The gray shaded region denotes values of $\log_{10}(f_{\rm Edd}) \leqslant -6$. We learn that both cold-mode and secular instability accretion dominate at high redshift.

bolometric AGN luminosity across redshift from X. Shen et al. (2020a; Figure 3).

4. Physics-based models converge with empirical estimates around $10^{5-6}\,M_\odot$ Mpc^{-3} in the local black hole mass density despite large differences in their cosmic mass density histories. Most models match the observed black hole accretion rate density, except SANTA CRUZ at $z = 0$ and DARK SAGE at $z > 2$. The cosmic black hole accretion density in DARK SAGE peaks around $z = 4$, whereas all other physics-based models and observations peak near $z = 2$ (Figure 6).
5. Figure 7 dissects the black hole mass from different growth channels within DARK SAGE. At all redshifts, $M_{\rm BH} \sim 10^6\,M_\odot$ grow through secular instabilities. For the most-massive black holes at $z = 0$, BH–BH mergers contribute 60% of the final mass, while the cold-mode channel adds 38%. In most redshifts, the cold-mode channel contributes as much as 70% and as little as 18%.
6. DARK SAGE displays an increasing peak in super-Eddington accretion with increasing redshift, which is revealed to originate from cold-mode accretion and secular instabilities (Figure 9).

Most physics-based models generally calibrate to the local $M_{\rm BH}$–σ, $M_{\rm BH}$–M_*, or $M_{\rm BH}$–$M_{\rm bulge}$ relation, as discussed in Appendix A. Despite this, we reveal significant differences in the high- and low-mass ends of their BHMF, black hole mass growth histories, Eddington ratio distributions across redshift, and cosmic SMBH mass and accretion density. Several causes that likely account for these differences across models compared here are enumerated below.

1. Models are usually only calibrated loosely to reproduce observed local relations for "typical" SMBHs. However, there may be deviations at the lowest masses (from, e.g., supernova feedback) and the highest masses (from, e.g., SMBH mergers and the details of AGN feedback implementation).
2. Even observational and empirical inferences of local relationships vary significantly. Calibration becomes sensitive to which relationships are assumed between black hole mass and the properties of their hosts, and how the scatter in these scaling relations is treated.
3. Physics-based models (especially numerical hydrodynamics simulations) are usually only calibrated at $z = 0$, and there are many paths to reach the same final relationships.

We find that exactly which scaling relationship is used to infer the BHMF matters. E. Tundo et al. (2007), M. Bernardi et al. (2007), and T. R. Lauer et al. (2007) argued that the BHMF varies depending on whether the bulge mass or the velocity dispersion is used to relate the black hole mass to its host galaxy. Meanwhile, others claim that there are no significant differences in the observed scatter between $M_{\rm BH}$–σ and $M_{\rm BH}$–$M_{\rm bulge}$ in massive ellipticals (N. J. McConnell & C.-P. Ma 2013; N. Sahu et al. 2019). The local BHMF is estimated based on the distribution of host galaxy properties, assuming that black hole masses follow a constant log-normal scatter around a single-power-law scaling relationship. Recent observations, however, suggest that this assumption may not hold true, indicating that the correlations break down at the highest and lowest black hole masses (T. R. Lauer et al. 2007;

K. Gültekin et al. 2009; B. C. Kelly & A. Merloni 2012). This could introduce biases in the BHMF derived from these scaling relationships, which subsequently affect the BHMF estimated from the continuity equation. Therefore, it is crucial to obtain more direct $M_{\rm BH}$ estimates through dynamical and kinematic modeling for a diverse range of galaxy types, particularly at the extremes of the $M_{\rm BH}$ spectrum. However, in the current state of the field, statistically abundant derivations of black hole masses through direct dynamical and kinematic modeling is observationally expensive. Recent efforts focus on indirect black hole mass measurements, which are highly effective (D. Savić et al. 2018; Gravity+ Collaboration et al. 2022; V. Ramakrishnan et al. 2023; J. Hernández-Yévenes et al. 2024).

When constructing models of SMBH evolution, we often trade off between physical realism and the match to observational data in each physical aspect tackled in the modeling process. Although empirical models like TRINITY can reproduce all observational data considered by construction, physics-based models such as the SANTA CRUZ SAM and ILLUSTRISTNG unexpectedly match observed high-redshift properties and trends, including the BHMF, bolometric AGN luminosity, and cosmic SMBH mass and accretion rate history, despite not being explicitly calibrated to them. Our study highlights that much of the discrepancy in, for example the BHMF, between observations and physics-based models are attributed to differences in SMFs and scaling relations adopted in calibrating the models.

Throughout this study, the outlier in the BHMF, bolometric AGN luminosity function, and the cosmic SMBH mass and accretion rate density at high redshift has been DARK SAGE. The bump near $M_{\rm BH} \approx 10^8\,M_\odot$ found in the BHMF above $z = 2$ is imprinted in the bolometric AGN luminosity function. Surprisingly, by $z = 5$–6, it matches the inferred bolometric AGN luminosity from “little red dots” (H. B. Akins et al. 2024). We caution about the interpretation of such a bump, as this could be a resolution effect from the lack of low halo masses. The distinct shape of DARK SAGE BHMF likely arises from a high black hole occupation fraction (seeding a central black hole in every galaxy) and allowing super-Eddington accretion, enabling many black holes to grow into SMBHs. From dissecting the black hole mass growth channel contributions in DARK SAGE, we know that the cold-mode growth commonly dominates the SMBH mass budget in the high-redshift Universe, a result consistent with S. Amarantidis et al. (2019). For $M_{\rm BH} \approx 10^8\,M_\odot$, the mass acquired from the cold-mode channel is about 80% of the total mass at $z = 5$–6. The amount of cold-mode growth can be manually adjusted using the free parameter $f_{\rm BH}$. Lowering $f_{\rm BH}$ reduces the pronounced bump at $L_{\rm bol} \sim 10^{46}$ erg s^{-1} above $z = 2$, leading to a better match with the physics-based models and the bolometric AGN luminosity function from X. Shen et al. (2020a). Matching the AGN luminosity function from H. B. Akins et al. (2024) suggests that if these “little red dots” are AGNs, their growth may be strongly tied to galaxy mergers.

Interestingly, using the semianalytic model Cosmic Archaeology Tool (CAT; A. Trinca et al. 2022, 2023, 2024a), A. Trinca et al. (2024b) found that super-Eddington accretion leads to a rise of the AGN bolometric luminosity function at $L_{\rm bol} > 10^{45}$ erg s^{-1}, driven by a population of low-mass black holes undergoing brief episodes of rapid growth. Similarly to predictions from DARK SAGE, CAT shows a decrease in the bolometric luminosity function at the bright end by more than 2 orders of magnitude compared to the number density estimated by H. B. Akins et al. (2024) at the bright end of the distribution for $L_{\rm bol} \geqslant 10^{46.5}$ erg s^{-1}.

In DARK SAGE, the accretion density declines at $\log M_{\rm h} > 12$ due to the exclusion of significant low-mass, super-Eddington accreting black holes. Since the majority of low-mass black holes in DARK SAGE accrete above the Eddington limit for $z > 3$ (see Figure 5), the model diverges significantly from others such as SANTA CRUZ, RN18, and TNG. Observational estimates and most theoretical models typically assume Eddington-limited growth, leading to smaller predicted deviations in accretion density. If the AGNs identified by H. B. Akins et al. (2024) are indeed accreting at super-Eddington, both models and observations likely underpredict the accretion density at $z \sim 6$ by at least an order of magnitude.

As suggested above, a caveat to our results is that the mass contribution from cold-mode, merger-driven, and secular instabilities in DARK SAGE depends on the value chosen for $f_{\rm BH}$. For example, reducing $f_{\rm BH}$ to 3% increases the contribution from merger-driven instability at all redshifts because more mass is added to the galactic disk, triggering starburst episodes and allowing the galaxy to grow in stellar mass. Therefore, any unstable gas with low angular momentum is added to the primary black hole. This also affects secular instabilities since galaxies that have regulated instabilities after a merger are likely to have larger cold gas reservoirs, which increases the likelihood of this gas becoming unstable over time. Lower values of $f_{\rm BH}$ for $z < 2$ allow black holes with $M_{\rm BH} \sim 10^6\,M_\odot$ to primarily gain their mass through the cold-mode channel, rather than through secular instabilities. This is because galaxies can regulate their instabilities and grow their stellar mass more efficiently relative to their black hole mass. For more-massive black holes, contributions from secular and merger-driven instabilities become more significant.

Several observational studies support the idea that much of the rapid black hole accretion is triggered by cold gas streams from minor galaxy mergers and secular instabilities rather than major galaxy mergers, especially for late-type galaxies (P. F. Hopkins & L. Hernquist 2006; A. Georgakakis et al. 2009; F. Bournaud et al. 2012; V. Marian et al. 2019; E. L. Lambrides et al. 2021). R. S. Sharma et al. (2024) showed that AGN activity is generally not driven by major mergers, except for a few gas-rich mergers at $z < 0.9$. Major mergers do not contribute significantly to the growth of central SMBHs, resulting in their central black holes not sustaining long-term accretion. This is important given that, in DARK SAGE, much of the cold-mode accretion in the early stages of black hole growth comes from cold gas from minor galaxy mergers. This is partially supported by studies showing that, in the early stages of galaxy growth, cold flows dominate the growth of the disk (A. M. Brooks et al. 2009; A. Dekel et al. 2009; N. Bouché et al. 2010; F. van de Voort et al. 2012; M. Noguchi 2018; Z. Kocjan et al. 2024; S. Waterval et al. 2025). Rapid black hole accretion driven by cold gas streams and secular instabilities might explain the lack of a stronger observational link between major galaxy mergers and AGN activity.

Although the division of black hole growth channels in DARK SAGE is similar to other semianalytic models

(R. S. Somerville et al. 2008; A. J. Benson 2012; D. J. Croton et al. 2016), its main distinction lies in the treatment of instabilities. While instabilities do not physically happen in annuli, as calculated in DARK SAGE, the model behaves more like a global prescription. Because most unstable mass is transferred inward, if annulus *i* becomes unstable, it increases the likelihood that annulus *i-1* will also become unstable. Since we check annulus *i-1* next, this instability can cascade all the way to the center of the galaxy, effectively resembling a global instability.

When tracing SMBHs at $z > 6$, two distinct populations of host galaxies emerge: those that have not experienced any mergers, resulting in both their galaxies and black holes growing through secular accretion, and those that have undergone minor mergers and a few major mergers. The latter population benefits from ex situ accretion, allowing black holes to gain mass through the cold-mode channel and merger-driven instabilities. We limit our discussion of black holes and galaxies above $z > 6$, due to the insufficient resolution of Millennium merger trees in capturing low-mass halos and galaxy mergers.

Our results highlight the diversity of black hole growth histories explored across models. We use the semianalytic model DARK SAGE to separate the SMBH assembly into its multiple different growth channels across redshift. Low-mass black holes in DARK SAGE primarily grow via secular instabilities. Most of the mass for black holes above $M_{\rm BH} \sim 10^7\,M_\odot$ comes from the cold-mode growth channel. At the lowest redshifts, BH–BH mergers contribute up to 60% its current mass. We interpret the mass assembly of DARK SAGE black holes as initially undergoing a super-Eddington growth phase, followed by a gradual decrease in Eddington ratio as their mass increases. As O. Piana et al. (2024) highlights, while super-Eddington and Eddington-limited accretion models match the observed SMBHs and host galaxy properties at $z = 5$–7, they diverge at higher redshifts and in the intermediate-mass range. In DARK SAGE, many black holes may have experienced stalled growth following their initial episode of super-Eddington accretion resulting in a population of undermassive black holes at later times. Several models incorporate super-Eddington accretion onto stellar-mass black holes, suggesting that such accretion is possible under certain conditions (A. Sądowski 2009; A. Sądowski et al. 2014, 2016; A. Sądowski & R. Narayan 2016; K. Inayoshi et al. 2020; Y. Shi et al. 2024; A. Trinca et al. 2024b; F. Pacucci & R. Narayan 2024; S. T. Gordon et al. 2025; J. Jeon et al. 2025), though in some cases, supercritical disks can self-regulate to Eddington on General relativistic magnetohydrodynamic scales depending on the initial conditions (P. C. Fragile et al. 2025).

Furthermore, observational evidence also supports super-Eddington accretion (P. Du et al. 2018). In DARK SAGE, super-Eddington accretion results from Toomre instabilities, which are dependent on our assumption for the velocity dispersion of the gas in the galaxy disk. Lower sound speeds result in lower Toomre-Q values, making disks more prone to intense, centrally concentrated bursts of star formation. This compaction in galaxies, allowed by DARK SAGE, is affected by the angular momentum of infalling gas, determined by accretion from the halo and independent of disk dynamics. As a result, DARK SAGE galaxies experience a broad range of outcomes, with many undergoing compaction. Although these bursts might explain compact star-forming systems at $z \sim 2$, models that incorporate higher velocity dispersions due to disk instability generally result in less erratic evolution by allowing for some degree of self-regulation.

G. Lodato & P. Natarajan (2006) presented the formation of direct collapse black holes (DCBHs) using Toomre disk instabilities, a similar treatment to the one adopted in DARK SAGE with one key difference regarding outcome, i.e., disk fragmentation. Both models assume disk evolution is mainly driven by angular momentum redistribution induced by gravitational instabilities. While DARK SAGE grows $10^5\,M_\odot$ black holes above $z > 10$ with metal-poor gas, our work does not account for disk fragmentation. In DARK SAGE, the gas within an annulus is evenly distributed, and its starburst phase, along with its Toomre-Q criterion, is considered across the entire annulus. Yet, our model presents a promising path toward DCBH formation with super-Eddington accreted gas. This will be explored further in future works.

The diversity of SMBH assembly histories in the models considered here may be distinguishable by their resultant spin distributions, which encode information about recent growth by mergers and accretion (e.g., E. Berti & M. Volonteri 2008). Present X-ray reflection spectroscopy constraints point toward high spins for most SMBHs with thin accretion disks (C. S. Reynolds 2021), and event-horizon-scale studies aim to constrain spins for up to tens of additional sources at (more typical) low Eddington ratios (A. Ricarte et al. 2023). We plan to investigate spin distributions in future work, as it will likely provide strong discrimination between models.

Acknowledgments

A.J.P.V. gratefully acknowledges the overlapped support of a Postdoctoral fellowship from the Heising–Simons foundation and the National Science Foundation Astronomy & Astrophysics Postdoctoral Fellowship. This material is based on work supported by the National Science Foundation under award No. 2502826. A.J.P.V. also thanks John C. Forbes, Colin Burke, Tonima Ananna, and Meg Urry for helpful comments and discussions that inspired this manuscript. We used computational facilities from the Vanderbilt Advanced Computing Center for Research and Education (ACCRE) and the Yale Center for Research Computing (YCRC). Literature reviews for this work were made using NASA's Astrophysics Data System. P.N. and A.R. acknowledge support from the Gordon and Betty Moore Foundation and the John Templeton Foundation that fund the Black Hole Initiative (BHI) at Harvard University. The Flatiron Institute is a division of the Simons Foundation.

Software: IPython (F. Pérez & B. E. Granger 2007), Scipy (P. Virtanen et al. 2020), matplotlib (J. D. Hunter 2007), Astropy (T. P. Robitaille et al. 2013), NumPy (S. Van Der Walt et al. 2011)

Appendix A
Model Calibration

Calibrating models prior to comparison is crucial, as any differences might lead to inconsistencies between models. DARK SAGE employs prescriptions containing free parameters, whose values are determined through model calibration. Specifically, in this version of DARK SAGE, only eight free parameters are allowed to vary during the calibration process.

This calibration is manually conducted using a set of observational constraints, including the stellar mass function (I. K. Baldry et al. 2008), H I (M. A. Zwaan et al. 2005) and H2 mass functions (D. Keres et al. 2003), the H I–stellar mass scaling relation (T. Brown et al. 2015), the black hole–bulge mass relation (N. Scott et al. 2013), the Baryonic Tully–Fisher relation (D. V. Stark et al. 2009), the galaxy mass–metallicity relation (C. A. Tremonti et al. 2004), and the mean cosmic star formation density–redshift relation (R. S. Somerville et al. 2001). All of these, with the exception of the mean cosmic star formation density–redshift relation, are adopted from $z = 0$. Further details can be found in Appendix A of A. R. H. Stevens et al. (2016).

RN18 explored several models with three to five tuned parameters. Here, we use the power-law model, which assigns to SMBHs a random Eddington ratio drawn from a power-law distribution. This model uses five parameters tuned to reproduce the $z = 0.1$ AGN bolometric luminosity function (P. F. Hopkins et al. 2007b; Y. Ueda et al. 2014) and the local M–σ relation (R. P. Saglia et al. 2016). To obtain realistic scatter for the black hole mass and luminosity functions, RN18 calibrated to the local SMBH mass function, by manually adjusting the scatter to achieve a satisfactory alignment with acceptable mass function estimates from F. Shankar et al. (2009; see Appendix B of RN18).

The SANTA CRUZ SAM contains around 25 free parameters that are calibrated by hand to match a set of observations at $z = 0$. These observations include: the stellar mass function (M. Bernardi et al. 2013), the ratio of stellar mass to halo mass as a function of halo mass (A. Rodríguez-Puebla et al. 2017), the cold gas fraction (defined as $f_{\mathrm{cold}} \equiv (M_{\mathrm{HI}} + M_{\mathrm{H2}})/M_*$) as a function of stellar mass for disk-dominated galaxies (defined as having bulge-to-total stellar mass ratios $\mathrm{B/T} < 0.4$; M. S. Peeples et al. 2014; A. R. Calette et al. 2018), the stellar metallicity as a function of stellar mass (A. Gallazzi et al. 2005), and the black hole mass–bulge mass relation (N. J. McConnell & C.-P. Ma 2013; see Appendix B of L. Y. A. Yung et al. 2019; A. Gabrielpillai et al. 2022).

The ILLUSTRISTNG simulation is tuned to match the stellar mass function, the stellar mass–halo mass relation, the total gas mass content within the virial radius (r500) of massive groups, the stellar mass–stellar size relation, and the black hole–galaxy mass relation all at $z = 0$, in addition to the cosmic SFR density up to $z = 10$ (see A. Pillepich et al. 2018).

TRINITY contains 56 parameters calibrated by an MCMC to fit the observed stellar mass function from $z = 0$–8, the galaxy quenched fractions from $z = 0$–4, cosmic SFRs from $z = 0$–10, specific SFRs from $z = 0$–9, galaxy UV luminosity functions from $z = 9$–10, quasar luminosity functions from $z = 0$–5, quasar probability distribution functions from $z = 0 - 2.5$, active SMBH mass function from $z = 0$–5, SMBH mass–bulge mass relation at $z = 0$, and the SMBH mass distribution of bright quasars from $z = 5.8$–6.5 (see the observational references used in Tables 4–10 of H. Zhang et al. 2023).

As stated here, TRINITY is the only model that is tuned to follow scaling relations at high redshift, whereas the SANTA CRUZ SAM and (RN18) are calibrated to $z = 0$ observations. DARK SAGE and ILLUSTRISTNG are calibrated to match the observed cosmic star formation history. While there is some overlap in the calibration quantities used for the SAMs and ILLUSTRISTNG, each method also incorporates distinct observational data not used by the other. Furthermore, the specific observational studies chosen for calibration differ between techniques in some cases. Although quantifying differences in calibration procedures is ideal, it is an expensive task that requires further work beyond this paper. Nonetheless, current model predictions that match a set of observations still yield valuable results.

Appendix B
Eddington Ratio Distributions Binned by Halo Mass

Figure 10 shows the Eddington ratio distributions similar to Figure 5, but here we break down all galaxies into bins of halo masses. At $z = 0$, DARK SAGE shows a trimodal distribution with peaks at $\log_{10}(f_{\mathrm{Edd}}) \sim -6, \; -5.5$ and -4.5. The peak at $\log_{10}(f_{\mathrm{Edd}}) \sim -6$ is primarily contributed by galaxies with halo masses around $M_h \sim 10^{12-13}$, $M_{\odot}$. The peak at $\log 10(f_{\mathrm{Edd}}) \sim -5.5$ is driven by galaxies with $M_h \sim 10^{14}$, $M_{\odot}$, while the peak at $\log 10(f_{\mathrm{Edd}}) \sim -4.5$ corresponds to black holes in low-mass halos. The SANTA CRUZ SAM displays a narrow distribution around $\log 10(f_{\mathrm{Edd}}) \sim -4$ at $z = 0$, which is heavily composed of black holes in low-mass halos. Interestingly, at $z > 3$, black holes in galaxies with $M_h \sim 10^{12-14} M_{\odot}$ exhibit a bimodal Eddington ratio distribution. The first peak ranges from $\log 10(f_{\mathrm{Edd}}) \sim -4$ to -3, while the second peak spans from $\log_{10}(f_{\mathrm{Edd}}) \sim -1$ to 1. We find that the first peak dominates at all redshifts and halo masses. The RN18 model shows consistent Eddington distributions across redshift and halo mass. TNG300-1 shows a broad distribution that peaks around $\log_{10}(f_{\mathrm{Edd}}) \sim -2$. Black holes in $M_h \sim 10^{12} M_{\odot}$ drive such high $\log_{10}(f_{\mathrm{Edd}})$. At fixed z, this peak in the Eddington ratio distribution is consistent across all halo mass bins (see Appendix B).

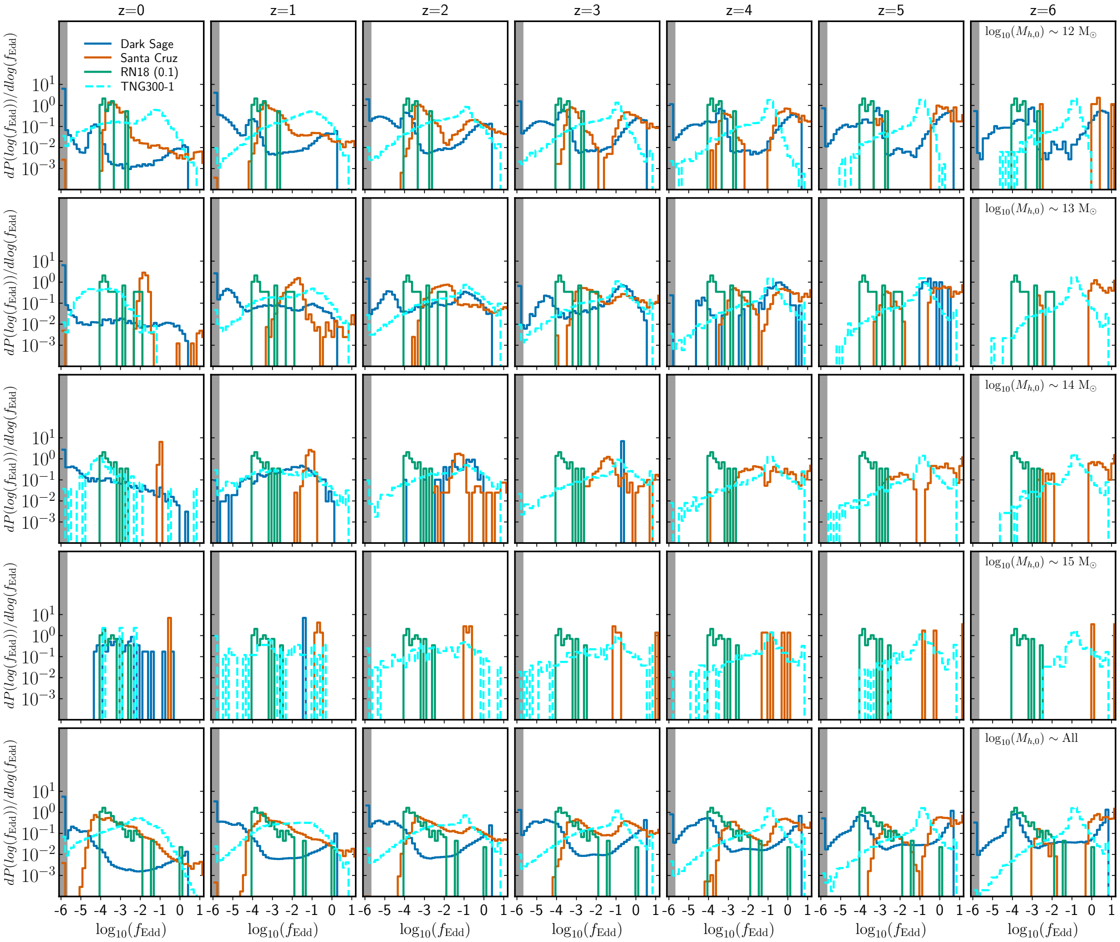

Figure 10. Histograms of the Eddington ratio distributions are shown for Dark Sage (solid dark-blue line), the Santa Cruz SAM (solid brown line), and RN18 (solid green line with $p_{\rm merge} = 0.1$). The RN18 model with $p_{\rm merge} = 1.0$ has similar Eddington ratio distributions to the $p_{\rm merge} = 0.1$ model, so only one is presented. These models are compared to TNG300-1 (dashed cyan line). The gray shaded region denote values of $\log_{10}(f_{\rm Edd}) \leqslant -6$. Each column shows varying redshifts from $z = 0$ (first column) up to $z = 6$ (last column). Each row shows different halo mass bins from $\sim 10^{12}\, M_\odot$(first row) to $\sim 10^{15}\, M_\odot$ (fourth row). The last row shows all halo masses combined. The data displayed in the figures show the largest progenitor galaxy for a root $\log_{10}(M_h) \sim 12 - 15$ at $z = 0$. All models show a diversity of Eddington ratio distributions across halo masses and redshifts.

ORCID iDs

Antonio J. Porras-Valverde https://orcid.org/0000-0002-1996-0445

Angelo Ricarte https://orcid.org/0000-0001-5287-0452

Priyamvada Natarajan https://orcid.org/0000-0002-5554-8896

Rachel S. Somerville https://orcid.org/0000-0002-6748-6821

Austen Gabrielpillai https://orcid.org/0000-0003-4295-3793

L. Y. Aaron Yung https://orcid.org/0000-0003-3466-035X

References

Abramowicz, M. A., Czerny, B., Lasota, J. P., & Szuszkiewicz, E. 1988, ApJ, 332, 646
Agazie, G., Anumarlapudi, A., Archibald, A. M., et al. 2023, ApJL, 952, L37
Akins, H. B., Casey, C. M., Lambrides, E., et al. 2025, ApJ, 991, 37
Aller, M. C., & Richstone, D. O. 2007, ApJ, 665, 120
Amarantidis, S., Afonso, J., Messias, H., et al. 2019, MNRAS, 485, 2694
Ananna, T. T., Bogdán, Á., Kovács, O. E., Natarajan, P., & Hickox, R. C. 2024, ApJL, 969, L18
Ananna, T. T., Treister, E., Urry, C. M., et al. 2019, ApJ, 871, 240
Ananna, T. T., Urry, C. M., Treister, E., et al. 2020, ApJ, 903, 85
Baldry, I. K., Driver, S. P., Loveday, J., et al. 2012, MNRAS, 421, 621
Baldry, I. K., Glazebrook, K., & Driver, S. P. 2008, MNRAS, 959, 945
Barger, A. J., Cowie, L. L., Mushotzky, R. F., et al. 2005, AJ, 129, 578
Begelman, M. C. 1979, MNRAS, 187, 237
Begelman, M. C., & Nath, B. B. 2005, MNRAS, 361, 1387
Behroozi, P., Wechsler, R. H., Hearin, A. P., & Conroy, C. 2019, MNRAS, 488, 3143
Behroozi, P. S., Wechsler, R. H., & Wu, H.-Y. 2013a, ApJ, 762, 109
Behroozi, P. S., Wechsler, R. H., Wu, H.-Y., et al. 2013b, ApJ, 763, 18
Beifiori, A., Courteau, S., Corsini, E. M., & Zhu, Y. 2012, MNRAS, 419, 2497
Benson, A. J. 2012, NewA, 17, 175
Bernardi, M., Fischer, J. L., Sheth, R. K., et al. 2017a, MNRAS, 468, 2569
Bernardi, M., Meert, A., Sheth, R. K., et al. 2017b, MNRAS, 467, 2217
Bernardi, M., Meert, A., Sheth, R. K., et al. 2013, MNRAS, 436, 697
Bernardi, M., Shankar, F., Hyde, J. B., et al. 2010, MNRAS, 404, 2087
Bernardi, M., Sheth, R. K., Fischer, J. L., et al. 2018, MNRAS, 475, 757
Bernardi, M., Sheth, R. K., Tundo, E., & Hyde, J. B. 2007, ApJ, 660, 267
Berti, E., & Volonteri, M. 2008, ApJ, 684, 822
Binney, J., & Tremaine, S. 1987, Galactic Dynamics (Princeton, NJ: Princeton Univ. Press)
Bogdán, Á., Goulding, A. D., Natarajan, P., et al. 2024, NatAs, 8, 126
Bondi, H. 1952, MNRAS, 112, 195
Booth, C. M., & Schaye, J. 2009, MNRAS, 398, 53
Bose, S., Eisenstein, D. J., Hernquist, L., et al. 2019, MNRAS, 490, 5693
Bouché, N., Dekel, A., Genzel, R., et al. 2010, ApJ, 718, 1001
Bournaud, F., Juneau, S., Le Floc'h, E., et al. 2012, ApJ, 757, 81
Boylan-Kolchin, M., Bullock, J. S., Sohn, S. T., Besla, G., & van der Marel, R. P. 2013, ApJ, 768, 140
Boylan-Kolchin, M., Ma, C.-P., & Quataert, E. 2008, MNRAS, 383, 93
Brooks, A. M., Governato, F., Quinn, T., Brook, C. B., & Wadsley, J. 2009, ApJ, 694, 396

Brown, T., Catinella, B., Cortese, L., et al. 2015, MNRAS, 452, 2479
Burke, C. J., Natarajan, P., Baldassare, V. F., & Geha, M. 2025, ApJ, 978, 77
Calette, A. R., Avila-Reese, V., Rodríguez-Puebla, A., Hernández-Toledo, H., & Papastergis, E. 2018, RMxAA, 54, 443
Cattaneo, A., Blaizot, J., Devriendt, J., & Guiderdoni, B. 2005, MNRAS, 364, 407
Cavaliere, A., Morrison, P., & Wood, K. 1971, ApJ, 170, 223
Ciotti, L., & Ostriker, J. P. 2001, ApJ, 551, 131
Colín, P., Klypin, A. A., Kravtsov, A. V., & Khokhlov, A. M. 1999, ApJ, 523, 32
Conroy, C., & Wechsler, R. H. 2009, ApJ, 696, 620
Cox, T. J., Jonsson, P., Primack, J. R., & Somerville, R. S. 2006, MNRAS, 373, 1013
Cox, T. J., Jonsson, P., Somerville, R. S., Primack, J. R., & Dekel, A. 2008, MNRAS, 384, 386
Croton, D. J., Springel, V., White, S. D., et al. 2006, MNRAS, 365, 11
Croton, D. J., Stevens, A. R. H., Tonini, C., et al. 2016, ApJS, 222, 22
Dattathri, S., Natarajan, P., Porras-Valverde, A. J., et al. 2025, ApJ, 984, 122
Davidge, H., Serjeant, S., Pearson, C., et al. 2017, MNRAS, 472, 4259
Dekel, A., Birnboim, Y., Engel, G., et al. 2009, Natur, 457, 451
Di Matteo, T., Colberg, J., Springel, V., Hernquist, L., & Sijacki, D. 2008, ApJ, 676, 33
Driver, S. P., Hill, D. T., Kelvin, L. S., et al. 2011, MNRAS, 413, 971
Driver, S. P., Bellstedt, S., Robotham, A. S. G., et al. 2022, MNRAS, 513, 439
Du, P., Zhang, Z.-X., Wang, K., et al. 2018, ApJ, 856, 6
Efstathiou, G., Lake, G., & Negroponte, J. 1982, MNRAS, 199, 1069
Fabian, A. C. 1999, MNRAS, 308, L39
Fouqué, P., Solanes, J. M., Sanchis, T., & Balkowski, C. 2001, A&A, 375, 770
Fragile, P. C., Middleton, M. J., Bollimpalli, D. A., & Smith, Z. 2025, MNRAS, 540, 2820
Gabor, J. M., Impey, C. D., Jahnke, K., et al. 2009, ApJ, 691, 705
Gabrielpillai, A., Somerville, R. S., Genel, S., et al. 2022, MNRAS, 517, 6091
Gallazzi, A., Charlot, S., Brinchmann, J., White, S. D. M., & Tremonti, C. A. 2005, MNRAS, 362, 41
Gebhardt, K., Bender, R., Bower, G., et al. 2000, ApJL, 539, L13
Genel, S., Vogelsberger, M., Springel, V., et al. 2014, MNRAS, 445, 175
Georgakakis, A., Coil, A. L., Laird, E. S., et al. 2009, MNRAS, 397, 623
Gordon, S. T., Smith, B. D., Khochfar, S., & Beckmann, R. S. 2025, MNRAS, 537, 674
Graham, A. W., Driver, S. P., Allen, P. D., & Liske, J. 2007, MNRAS, 378, 198
Graham, A. W., Erwin, P., Caon, N., & Trujillo, I. 2001, ApJL, 563, L11
Gravity+ Collaboration, Abuter, R., Alarcon, P., et al. 2022, Msngr, 189, 17
Greene, J. E., Labbe, I., Goulding, A. D., et al. 2024, ApJ, 964, 39
Greene, J. E., Strader, J., & Ho, L. C. 2020, ARA&A, 58, 257
Gruppioni, C., Pozzi, F., Zamorani, G., & Vignali, C. 2011, MNRAS, 416, 70
Gu, M., Greene, J. E., Newman, A. B., et al. 2022, ApJ, 932, 103
Gültekin, K., Richstone, D. O., Gebhardt, K., et al. 2009, ApJ, 698, 198
Guo, J., Onoue, M., Inayoshi, K., et al. 2025, ApJ, 991, 74
Guyon, O., Sanders, D. B., & Stockton, A. 2006, ApJS, 166, 89
Habouzit, M., Onoue, M., Bañados, E., et al. 2022a, MNRAS, 511, 3751
Habouzit, M., Somerville, R. S., Li, Y., et al. 2022b, MNRAS, 509, 3015
Haehnelt, M. G., & Kauffmann, G. 2000, MNRAS, 318, L35
Haehnelt, M. G., Natarajan, P., & Rees, M. J. 1998, MNRAS, 300, 817
Harikane, Y., Zhang, Y., Nakajima, K., et al. 2023, ApJ, 959, 39
Häring, N., & Rix, H.-W. 2004, ApJL, 604, L89
He, W., Akiyama, M., Enoki, M., et al. 2024, ApJ, 962, 152
Hearin, A. P., & Watson, D. F. 2013, MNRAS, 435, 1313
Henriques, B. M. B., White, S. D. M., Thomas, P. A., et al. 2015, MNRAS, 451, 2663
Hernández-Yévenes, J., Nagar, N., Arratia, V., & Jarrett, T. H. 2024, MNRAS, 531, 4503
Hirschmann, M., Somerville, R. S., Naab, T., & Burkert, A. 2012, MNRAS, 426, 237
Hopkins, P. F., & Hernquist, L. 2006, ApJS, 166, 1
Hopkins, P. F., Hernquist, L., Cox, T. J., Robertson, B., & Krause, E. 2007a, ApJ, 669, 45
Hopkins, P. F., Hernquist, L., Cox, T. J., et al. 2005a, ApJ, 630, 716
Hopkins, P. F., Hernquist, L., Martini, P., et al. 2005b, ApJL, 625, L71
Hopkins, P. F., Richards, G. T., & Hernquist, L. 2007b, ApJ, 654, 731
Hunter, J. D. 2007, CSE, 9, 90
Inayoshi, K., Visbal, E., & Haiman, Z. 2020, ARA&A, 58, 27
Izquierdo-Villalba, D., Sesana, A., Colpi, M., et al. 2024, A&A, 686, A183
Jeon, J., Liu, B., Taylor, A. J., et al. 2025, ApJ, 988, 110
Joshi, G. D., Pillepich, A., Nelson, D., et al. 2020, MNRAS, 496, 2673
Kashibadze, O. G., Karachentsev, I. D., & Karachentseva, V. E. 2020, A&A, 635, A135
Kauffmann, G., & Haehnelt, M. 2000, MNRAS, 311, 576
Kelly, B. C., & Merloni, A. 2012, AdAst, 2012, 970858
Kelly, B. C., Sobolewska, M., & Siemiginowska, A. 2011, ApJ, 730, 52
Keres, D., Yun, M. S., & Young, J. S. 2003, ApJ, 582, 659
Khandai, N., Di Matteo, T., Croft, R., et al. 2015, MNRAS, 450, 1349
Kim, S. J., Goto, T., Ling, C.-T., et al. 2024, MNRAS, 527, 5525
Klypin, A., Zhao, H., & Somerville, R. S. 2002, ApJ, 573, 597
Kocevski, D. D., Barro, G., McGrath, E. J., et al. 2023a, ApJL, 946, L14
Kocevski, D. D., Onoue, M., Inayoshi, K., et al. 2023b, ApJL, 954, L4
Kocjan, Z., Cadiou, C., Agertz, O., & Pontzen, A. 2024, MNRAS, 534, 918
Kokorev, V., Caputi, K. I., Greene, J. E., et al. 2024, ApJ, 968, 38
Kormendy, J., & Ho, L. C. 2013, ARA&A, 51, 511
Kormendy, J., & Richstone, D. 1995, ARA&A, 33, 581
Kovács, O. E., Bogdán, Á., Natarajan, P., et al. 2024, ApJL, 965, L21
Kravtsov, A. V., Berlind, A. A., Wechsler, R. H., et al. 2004, ApJ, 609, 35
Kroupa, P., Subr, L., Jerabkova, T., & Wang, L. 2020, MNRAS, 498, 5652
Kulessa, A. S., & Lynden-Bell, D. 1992, MNRAS, 255, 105
Labbe, I., Greene, J. E., Matthee, J., et al. 2024, arXiv:2412.04557
Lambrides, E. L., Chiaberge, M., Heckman, T., et al. 2021, ApJ, 919, 129
Lauer, T. R., Faber, S. M., Richstone, D., et al. 2007, ApJ, 662, 808
Leja, J., Speagle, J. S., Johnson, B. D., et al. 2020, ApJ, 893, 111
Liepold, E. R., & Ma, C.-P. 2024, ApJL, 971, L29
Ling, C.-T., Kim, S. J., Wu, C. K. W., et al. 2022, MNRAS, 517, 853
Ling, C.-T., Kim, S. J., Wu, C. K. W., et al. 2023, MNRAS, 522, 1138
Little, B., & Tremaine, S. 1987, ApJ, 320, 493
Lodato, G., & Natarajan, P. 2006, MNRAS, 371, 1813
Lodato, G., & Natarajan, P. 2007, MNRAS, 377, L64
Ma, C.-P., Greene, J. E., McConnell, N., et al. 2014, ApJ, 795, 158
Madau, P., & Haardt, F. 2024, ApJL, 976, L24
Magorrian, J., Tremaine, S., Richstone, D., et al. 1998, AJ, 115, 2285
Maiolino, R., Scholtz, J., Curtis-Lake, E., et al. 2024, A&A, 691, A145
Maiolino, R., Scholtz, J., Curtis-Lake, E., et al. 2024, A&A, 691, A145
Marconi, A., & Hunt, L. K. 2003, ApJL, 589, L21
Marconi, A., Risaliti, G., Gilli, R., et al. 2004, MNRAS, 351, 169
Marian, V., Jahnke, K., Mechtley, M., et al. 2019, ApJ, 882, 141
Marinacci, F., Vogelsberger, M., Pakmor, R., et al. 2018, MNRAS, 480, 5113
Martizzi, D., Vogelsberger, M., Torrey, P., et al. 2020, MNRAS, 491, 5747
Marulli, F., Branchini, E., Moscardini, L., & Volonteri, M. 2007, MNRAS, 375, 649
Mathews, W. G. 1978, ApJ, 219, 413
Matthee, J., Naidu, R. P., Brammer, G., et al. 2024, ApJ, 963, 129
Mazzolari, G., Gilli, R., Maiolino, R., et al. 2024, arXiv:2412.04224
McAlpine, S., Helly, J. C., Schaller, M., et al. 2016, A&C, 15, 72
McConnell, N. J., & Ma, C.-P. 2013, ApJ, 764, 184
McLure, R. J., & Dunlop, J. S. 2001, MNRAS, 327, 199
McLure, R. J., & Dunlop, J. S. 2002, MNRAS, 331, 795
Merloni, A. 2004, MNRAS, 353, 1035
Merloni, A., & Heinz, S. 2008, MNRAS, 388, 1011
Merritt, D., & Ferrarese, L. 2001, ApJ, 547, 140
Mezcua, M., Hlavacek-Larrondo, J., Lucey, J. R., et al. 2018, MNRAS, 474, 1342
Mezcua, M., Pacucci, F., Suh, H., Siudek, M., & Natarajan, P. 2024, ApJL, 966, L30
Mo, H. J., Mao, S., & White, S. D. M. 1998, MNRAS, 295, 319
Moster, B. P., Naab, T., & White, S. D. M. 2013, MNRAS, 428, 3121
Moster, B. P., Somerville, R. S., Maulbetsch, C., et al. 2010, ApJ, 710, 903
Moustakas, J., Coil, A. L., Aird, J., et al. 2013, ApJ, 767, 50
Murray, N., Quataert, E., & Thompson, T. A. 2005, ApJ, 618, 569
Naab, T., & Ostriker, J. P. 2017, ARA&A, 55, 59
Naiman, J. P., Pillepich, A., Springel, V., et al. 2018, MNRAS, 477, 1206
Nair, D. G., Nagar, N. M., Ramakrishnan, V., et al. 2024, in Proc. 16th EVN Symp., ed. E. Ros et al. (Bonn: Max-Planck-Institut für Radioastronomie), 75
Natarajan, P., Tang, K. S., McGibbon, R., et al. 2023, ApJ, 952, 146
Natarajan, P., & Treister, E. 2009, MNRAS, 393, 838
Nelson, D., Pillepich, A., Genel, S., et al. 2015, A&C, 13, 12
Nelson, D., Pillepich, A., Springel, V., et al. 2018, MNRAS, 475, 624
Nelson, D., Pillepich, A., Springel, V., et al. 2019, MNRAS, 490, 3234
Ni, Y., Di Matteo, T., Bird, S., et al. 2022, MNRAS, 513, 670
Nikolajuk, M., Papadakis, I. E., & Czerny, B. 2004, MNRAS, 350, L26
Noguchi, M. 2018, ApJ, 853, 67
Ntampaka, M., ZuHone, J., Eisenstein, D., et al. 2019, ApJ, 876, 82
Oliver, S. J., Goldschmidt, P., Franceschini, A., et al. 1997, MNRAS, 289, 471
Pacucci, F., & Loeb, A. 2020, ApJ, 895, 95

Pacucci, F., & Narayan, R. 2024, ApJ, 976, 96
Pacucci, F., Nguyen, B., Carniani, S., Maiolino, R., & Fan, X. 2023, ApJL, 957, L3
Parkinson, H., Cole, S., & Helly, J. 2008, MNRAS, 383, 557
Pearson, C. P., Oyabu, S., Wada, T., et al. 2010, A&A, 514, A8
Pearson, C. P., Serjeant, S., Oyabu, S., et al. 2014, MNRAS, 444, 846
Peeples, M. S., Werk, J. K., Tumlinson, J., et al. 2014, ApJ, 786, 54
Pérez, F., & Granger, B. E. 2007, CSE, 9, 21
Pérez-González, P. G., Barro, G., Rieke, G. H., et al. 2024, ApJ, 968, 4
Pesce, D. W., Palumbo, D. C. M., Narayan, R., et al. 2021, ApJ, 923, 260
Piana, O., Pu, H.-Y., & Wu, K. 2024, MNRAS, 530, 1732
Pillepich, A., Nelson, D., Hernquist, L., et al. 2018, MNRAS, 475, 648
Pillepich, A., Springel, V., Nelson, D., et al. 2018, MNRAS, 473, 4077
Planck Collaboration, Ade, P. A. R., Aghanim, N., et al. 2016, A&A, 594, A13
Porter, L. A., Somerville, R. S., Primack, J. R., & Johansson, P. H. 2014, MNRAS, 444, 942
Press, W. H., & Schechter, P. 1974, ApJ, 187, 425
Pringle, J. E., & King, A. 2007, Astrophysical Flows (Cambridge: Cambridge Univ. Press)
Ramakrishnan, V., Nagar, N., Arratia, V., et al. 2023, Galax, 11, 15
Reines, A. E., & Volonteri, M. 2015, ApJ, 813, 82
Reynolds, C. S. 2021, ARA&A, 59, 117
Ricarte, A., & Natarajan, P. 2018, MNRAS, 474, 1995
Ricarte, A., Tiede, P., Emami, R., Tamar, A., & Natarajan, P. 2023, Galax, 11, 6
Ricarte, A., Tremmel, M., Natarajan, P., Zimmer, C., & Quinn, T. 2021, MNRAS, 503, 6098
Robertson, B., Cox, T. J., Hernquist, L., et al. 2006, ApJ, 641, 21
Robitaille, T. P., Tollerud, E. J., Greenfield, P., et al. 2013, A&A, 558, A33
Rocca-Volmerange, B., de Lapparent, V., Seymour, N., & Fioc, M. 2007, A&A, 475, 801
Rodríguez-Puebla, A., Primack, J. R., Avila-Reese, V., & Faber, S. M. 2017, MNRAS, 470, 651
Romeo, A. B., Agertz, O., & Renaud, F. 2023, MNRAS, 518, 1002
Romeo, A. B., & Wiegert, J. 2011, MNRAS, 416, 1191
Saglia, R. P., Opitsch, M., Erwin, P., et al. 2016, ApJ, 818, 47
Sahu, N., Graham, A. W., & Davis, B. L. 2019, ApJ, 876, 155
Sales, L. V., Navarro, J. F., Peñafiel, L., et al. 2020, MNRAS, 494, 1848
Salucci, P., Szuszkiewicz, E., Monaco, P., & Danese, L. 1999, MNRAS, 307, 637
Sanchez, N. N., Bellovary, J. M., Holley-Bockelmann, K., et al. 2018, ApJ, 860, 20
Sato-Polito, G., Zaldarriaga, M., & Quataert, E. 2023, arXiv:2312.06756
Savić, D., Goosmann, R., Popović, L. Č., Marin, F., & Afanasiev, V. L. 2018, A&A, 614, A120
Savorgnan, G. A. D., Graham, A. W., Marconi, A., & Sani, E. 2016, ApJ, 817, 21
Schutte, Z., Reines, A. E., & Greene, J. E. 2019, ApJ, 887, 245
Scott, N., Graham, A. W., & Schombert, J. 2013, ApJ, 768, 76
Serjeant, S., Oliver, S., Rowan-Robinson, M., et al. 2000, MNRAS, 316, 768
Shankar, F., Weinberg, D. H., & Miralda-Escudé, J. 2009, ApJ, 690, 20
Shankar, F., Weinberg, D. H., & Miralda-Escudé, J. 2013, MNRAS, 428, 421
Sharma, R. S., Choi, E., Somerville, R. S., et al. 2024, MNRAS, 527, 9461
Shaya, E. J., Tully, R. B., Hoffman, Y., & Pomarède, D. 2017, ApJ, 850, 207
Shen, J., Eadie, G. M., Murray, N., et al. 2022a, ApJ, 925, 1
Shen, X., Hopkins, P. F., Faucher-Giguère, C.-A., et al. 2020a, MNRAS, 495, 3252
Shen, X., Vogelsberger, M., Nelson, D., et al. 2022b, MNRAS, 510, 5560
Shen, X., Vogelsberger, M., Nelson, D., et al. 2020b, MNRAS, 495, 4747
Shi, Y., Kremer, K., & Hopkins, P. F. 2024, A&A, 691, A24
Sijacki, D., Vogelsberger, M., Genel, S., et al. 2015, MNRAS, 452, 575
Silk, J., Begelman, M. C., Norman, C., Nusser, A., & Wyse, R. F. G. 2024, ApJL, 961, L39
Silk, J., & Rees, M. J. 1998, A&A, 331, L1
Sądowski, A. 2009, ApJS, 183, 171
Sądowski, A., Lasota, J.-P., Abramowicz, M. A., & Narayan, R. 2016, MNRAS, 456, 3915
Sądowski, A., & Narayan, R. 2016, MNRAS, 456, 3929
Sądowski, A., Narayan, R., McKinney, J. C., & Tchekhovskoy, A. 2014, MNRAS, 439, 503
Small, T. A., & Blandford, R. D. 1992, MNRAS, 259, 725
Somerville, R. S., & Davé, R. 2015, ARA&A, 53, 51
Somerville, R. S., Hopkins, P. F., Cox, T. J., Robertson, B. E., & Hernquist, L. 2008, MNRAS, 391, 481
Somerville, R. S., Olsen, C., Yung, L. Y. A., et al. 2021, MNRAS, 502, 4858
Somerville, R. S., Popping, G., & Trager, S. C. 2015, MNRAS, 453, 4337
Somerville, R. S., & Primack, J. R. 1999, MNRAS, 310, 1087
Somerville, R. S., Primack, J. R., & Faber, S. M. 2001, MNRAS, 320, 504
Spergel, D. N., Verde, L., Peiris, H. V., et al. 2003, ApJS, 148, 175
Springel, V. 2005, MNRAS, 364, 1105
Springel, V., Pakmor, R., Pillepich, A., et al. 2018, MNRAS, 475, 676
Springel, V., White, S. D., Jenkins, A., et al. 2005, Natur, 435, 629
Springel, V., White, S. D., Tormen, G., & Kauffmann, G. 2001, MNRAS, 328, 726
Stark, D. V., Mcgaugh, S. S., & Swaters, R. A. 2009, AJ, 138, 392
Stevens, A. R. H., Croton, D. J., & Mutch, S. J. 2016, MNRAS, 461, 859
Stevens, A. R. H., Lagos, C. D. P., Obreschkow, D., & Sinha, M. 2018, MNRAS, 481, 5543
Stevens, A. R. H., Sinha, M., Rohl, A., et al. 2024, PASA, 41, e053
Sturm, M. R., & Reines, A. E. 2024, ApJ, 971, 173
Suh, H., Scharwächter, J., Farina, E. P., et al. 2025, NatAs, 9, 271
Tang, J.-J., Goto, T., Ohyama, Y., et al. 2019, MNRAS, 484, 2575
Taylor, A. J., Finkelstein, S. L., Kocevski, D. D., et al. 2025, ApJ, 986, 165
Terrazas, B. A., Bell, E. F., Pillepich, A., et al. 2020, MNRAS, 493, 1888
Toomre, A. 1964, ApJ, 139, 1217
Tortosa, A., Ricci, C., Ho, L. C., et al. 2023, MNRAS, 519, 6267
Tremaine, S., Gebhardt, K., Bender, R., et al. 2002, ApJ, 574, 740
Tremonti, C. A., Heckman, T. M., Kauffmann, G., et al. 2004, ApJ, 613, 898
Trinca, A., Schneider, R., Maiolino, R., et al. 2023, MNRAS, 519, 4753
Trinca, A., Schneider, R., Valiante, R., et al. 2024a, MNRAS, 529, 3563
Trinca, A., Schneider, R., Valiante, R., et al. 2022, MNRAS, 511, 616
Trinca, A., Valiante, R., Schneider, R., et al. 2024b, arXiv:2412.14248
Tundo, E., Bernardi, M., Hyde, J. B., Sheth, R. K., & Pizzella, A. 2007, ApJ, 663, 53
Ueda, Y., Akiyama, M., Hasinger, G., Miyaji, T., & Watson, M. G. 2014, ApJ, 786, 104
van de Voort, F., Schaye, J., Altay, G., & Theuns, T. 2012, MNRAS, 421, 2809
Van Der Walt, S., Colbert, S. C., & Varoquaux, G. 2011, CSE, 13, 22
Vestergaard, M., & Peterson, B. M. 2006, ApJ, 641, 689
Virtanen, P., Gommers, R., Oliphant, T. E., et al. 2020, NatMe, 17, 261
Vito, F., Brandt, W. N., Yang, G., et al. 2018, MNRAS, 473, 2378
Vogelsberger, M., Genel, S., Springel, V., et al. 2014a, Natur, 509, 177
Vogelsberger, M., Genel, S., Springel, V., et al. 2014b, MNRAS, 444, 1518
Vogelsberger, M., Nelson, D., Pillepich, A., et al. 2020, MNRAS, 492, 5167
Volonteri, M., Dubois, Y., Pichon, C., & Devriendt, J. 2016, MNRAS, 460, 2979
Volonteri, M., Haardt, F., & Madau, P. 2003, ApJ, 582, 559
Wandel, A., Peterson, B. M., & Malkan, M. A. 1999, ApJ, 526, 579
Waterval, S., Cannarozzo, C., & Macciò, A. V. 2025, MNRAS, 537, 2726
Wechsler, R. H., & Tinker, J. L. 2018, ARA&A, 56, 435
Weinberger, R., Springel, V., Hernquist, L., et al. 2017, MNRAS, 465, 3291
Weinberger, R., Springel, V., Pakmor, R., et al. 2018, MNRAS, 479, 4056
White, S. D. M., & Rees, M. J. 1978, MNRAS, 183, 341
Wolf, J., Nandra, K., Salvato, M., et al. 2023, A&A, 669, A127
Wright, E. L., Eisenhardt, P. R. M., Mainzer, A. K., et al. 2010, AJ, 140, 1868
Wu, C. K. W., Ling, C.-T., Goto, T., et al. 2023, MNRAS, 523, 5187
Wyithe, J. S. B., & Loeb, A. 2003, ApJ, 595, 614
Yang, G., Caputi, K. I., Papovich, C., et al. 2023, ApJL, 950, L5
Yang, X., Mo, H. J., & van den Bosch, F. C. 2003, MNRAS, 339, 1057
Yao, Y., Ravi, V., Gezari, S., et al. 2023, ApJL, 955, L6
York, D. G., Adelman, J., Anderson, J. E. J., et al. 2000, AJ, 120, 1579
Yung, L. Y. A., Somerville, R. S., Ferguson, H. C., et al. 2022, MNRAS, 515, 5416
Yung, L. Y. A., Somerville, R. S., Finkelstein, S. L., Popping, G., & Davé, R. 2019, MNRAS, 483, 2983
Yung, L. Y. A., Somerville, R. S., Finkelstein, S. L., et al. 2021, MNRAS, 508, 2706
Yung, L. Y. A., Somerville, R. S., Finkelstein, S. L., et al. 2023, MNRAS, 519, 1578
Zanisi, L., Shankar, F., Lapi, A., et al. 2020, MNRAS, 492, 1671
Zappacosta, L., Piconcelli, E., Fiore, F., et al. 2023, A&A, 678, A201
Zappacosta, L., Piconcelli, E., Giustini, M., et al. 2020, A&A, 635, L5
Zhang, H., Behroozi, P., Volonteri, M., et al. 2023, MNRAS, 518, 2123
Zhou, X.-L., Zhang, S.-N., Wang, D.-X., & Zhu, L. 2010, ApJ, 710, 16
Zwaan, M. A., Meyer, M. J., Staveley-Smith, L., & Webster, R. L. 2005, MNRAS, 359, L30